

## Climates of the Twentieth and Twenty-First Centuries Simulated by the NCAR Climate System Model

AIGUO DAI, T. M. L. WIGLEY, B. A. BOVILLE, J. T. KIEHL, AND L. E. BUJA

*National Center for Atmospheric Research,\* Boulder, Colorado*

(Manuscript received 3 November 1999, in final form 24 March 2000)

### ABSTRACT

The Climate System Model, a coupled global climate model without “flux adjustments” recently developed at the National Center for Atmospheric Research, was used to simulate the twentieth-century climate using historical greenhouse gas and sulfate aerosol forcing. This simulation was extended through the twenty-first century under two newly developed scenarios, a business-as-usual case (ACACIA-BAU,  $\text{CO}_2 \approx 710$  ppmv in 2100) and a  $\text{CO}_2$  stabilization case (STA550,  $\text{CO}_2 \approx 540$  ppmv in 2100). Here we compare the simulated and observed twentieth-century climate, and then describe the simulated climates for the twenty-first century. The model simulates the spatial and temporal variations of the twentieth-century climate reasonably well. These include the rapid rise in global and zonal mean surface temperatures since the late 1970s, the precipitation increases over northern mid- and high-latitude land areas, ENSO-induced precipitation anomalies, and Pole-midlatitude oscillations (such as the North Atlantic oscillation) in sea level pressure fields. The model has a cold bias ( $2^\circ\text{--}6^\circ\text{C}$ ) in surface air temperature over land, overestimates of cloudiness (by 10%–30%) over land, and underestimates of marine stratus clouds to the west of North and South America and Africa.

The projected global surface warming from the 1990s to the 2090s is  $\sim 1.9^\circ\text{C}$  under the BAU scenario and  $\sim 1.5^\circ\text{C}$  under the STA550 scenario. In both cases, the midstratosphere cools due to the increase in  $\text{CO}_2$ , whereas the lower stratosphere warms in response to recovery of the ozone layer. As in other coupled models, the surface warming is largest at winter high latitudes ( $\geq 5.0^\circ\text{C}$  from the 1990s to the 2090s) and smallest ( $\sim 1.0^\circ\text{C}$ ) over the southern oceans, and is larger over land areas than ocean areas. Globally averaged precipitation increases by  $\sim 3.5\%$  (3.0%) from the 1990s to the 2090s in the BAU (STA550) case. In the BAU case, large precipitation increases (up to 50%) occur over northern mid- and high latitudes and over India and the Arabian Peninsula. Marked differences occur between the BAU and STA550 regional precipitation changes resulting from interdecadal variability. Surface evaporation increases at all latitudes except for  $60^\circ\text{--}90^\circ\text{S}$ . Water vapor from increased tropical evaporation is transported into mid- and high latitudes and returned to the surface through increased precipitation there. Changes in soil moisture content are small (within  $\pm 3\%$ ). Total cloud cover changes little, although there is an upward shift of midlevel clouds. Surface diurnal temperature range decreases by about  $0.2^\circ\text{--}0.5^\circ\text{C}$  over most land areas. The 2–8-day synoptic storm activity decreases (by up to 10%) at low latitudes and over midlatitude oceans, but increases over Eurasia and Canada. The cores of subtropical jets move slightly up- and equatorward. Associated with reduced latitudinal temperature gradients over mid- and high latitudes, the wintertime Ferrel cell weakens (by 10%–15%). The Hadley circulation also weakens (by  $\sim 10\%$ ), partly due to the upward shift of cloudiness that produces enhanced warming in the upper troposphere.

### 1. Introduction

The earth’s climate system (the atmosphere, ocean, biosphere, etc.) has been altered by human activities (e.g., fossil fuel combustion and deforestation) in many ways. One of the consequences is a sharp rise in atmospheric concentrations of greenhouse gases ( $\text{CO}_2$ ,  $\text{CH}_4$ , etc.) and aerosols since the late-nineteenth century

(Watson et al. 1990; Schimel et al. 1996). A large number of climate model experiments predict substantial climate changes (including surface warming) in response to increased concentrations of  $\text{CO}_2$  and other greenhouse gases (e.g., Mitchell et al. 1990; Kattenberg et al. 1996). Because the atmospheric loading of greenhouse gases is likely to rise in the twenty-first century as a result of the expected growth in the world economy and population, meaningful predictions of climate changes in the next century have many practical applications (e.g., for impact assessments and to guide future emission controls).

Reliable predictions of future climates are, however, still a big challenge for climate researchers. They require a) comprehensive models of the earth’s climate system that include all of its major components and the inter-

---

\* The National Center for Atmospheric Research is sponsored by the National Science Foundation.

---

Corresponding author address: Aiguo Dai, National Center for Atmospheric Research, P.O. Box 3000, Boulder, CO 80307-3000.  
E-mail: adai@ucar.edu

actions among them in a realistic fashion, and b) reliable projections of future emissions of  $\text{CO}_2$ ,  $\text{CH}_4$ ,  $\text{SO}_2$ , halocarbons, and other trace gases. Various general circulation models (GCMs) of the earth's climate system, including those with coupled atmosphere, ocean, and land components, have been developed to study natural climate variability and the climate responses to increased greenhouse gas and aerosol loadings (see Mitchell et al. 1990 and Kattenberg et al. 1996, and references therein).

Because projections of future emissions usually have large uncertainties, a standard GCM experiment is to assume an arbitrary rate of increase for  $\text{CO}_2$ , such as a 1% compound increase per year (e.g., Manabe et al. 1991; Mitchell et al. 1995; Russell and Rind 1999; Boer et al. 2000; Meehl et al. 2000a,b). Climate changes from these experiments are not normally linked to specific years in the future and thus are not presented as quantitative predictions of future climates. Other GCM experiments (e.g., Cubasch et al. 1992; Roeckner et al. 1999) have predicted future climate changes using concentrations based on independently determined emission scenarios.

Here we used the recently developed National Center for Atmospheric Research (NCAR) Climate System Model (CSM) to predict the climate for the twenty-first century based on two newly developed scenarios of future emissions of  $\text{CO}_2$ ,  $\text{SO}_2$ , and other trace gases. The CSM is a comprehensive climate model with coupled atmosphere, ocean, land, and sea-ice components (Boville and Gent 1998). The CSM differs from many other coupled GCMs in that it does not require conventional "flux adjustments" to produce a stable surface climate. The two future emission scenarios, an existing policies (A Consortium for the Application of Climate Impacts Assessments Business As Usual, or ACACIA-BAU, henceforth BAU) scenario and a policy ( $\text{CO}_2$  stabilization, or STA550) scenario, were generated using an energy-economics model driven by regionally specific assumptions with regard to population growth, economic growth, energy use per capita, technology developments, etc. Both the model and forcing scenarios used here represent our current best knowledge. We believe, therefore, that our results provide one of the better-based estimates regarding climate changes in the twenty-first century in response to anthropogenic forcings of greenhouse gases and aerosols.

The CSM, like other coupled GCMs, still has deficiencies in simulating the complex variability of present day climate. These deficiencies result from our still imperfect understanding of many physical processes in the climate system (e.g., formation of clouds and precipitation), and our limited ability (e.g., computer resources) to adequately represent these processes in the model. In addition, the future emission projections we use, like all such projections, are derived by making various assumptions regarding future economic and population growth and therefore undoubtedly have large uncer-

tainties. Consequently, the climate changes for the twenty-first century reported in this study, as in other similar studies, have large uncertainties (especially regarding regional changes). They should be considered only as members within a wide spectrum of possibilities.

In the following, we first briefly describe the CSM and the simulations (section 2), and then describe how we developed the two future forcing scenarios (section 3). The CSM was first used to simulate the twentieth-century climate using historical forcings of greenhouse gases and aerosols. This simulated twentieth-century climate is compared with available observations in section 4. The predicted twenty-first-century climates are presented in section 5. A summary is given in section 6.

## 2. Model and simulations

The CSM is described in detail by Boville and Gent (1998) and other papers in that issue of the *Journal of Climate*. The CSM is a coupled global climate model consisting of an atmospheric GCM [the Community Climate Model Version 3 (CCM3); Kiehl et al. 1998], an ocean GCM [the NCAR CSM Ocean Model (NCOM); Gent et al. 1998], a land surface biophysics model (LSM 1.0; Bonan 1998), and a sea-ice model (Weatherly et al. 1998). These component models are coupled through a "flux coupler" (Bryan et al. 1996), which computes interfacial fluxes between components. The ocean component, NCOM, is a new model based on the Geophysical Fluid Dynamics Laboratory Modular Ocean Model (MOM-1.1)  $z$ -coordinate model incorporating new parameterizations of the effects of mesoscale eddies and the upper-ocean boundary layer. The version of the CSM used in this study is CSM-1.3 described in Boville et al. (2001), which incorporates several changes to either greatly reduce the deep ocean drift found in earlier versions of the CSM (through a reduction of the aerodynamic roughness length of sea ice) or add new capabilities for transient climate simulations (through an introduction of prognostic greenhouse gas distributions and an interactive sulfur cycle). The CSM has an equilibrium sensitivity of about  $2.1^\circ\text{C}$  global mean warming for a doubling of atmospheric  $\text{CO}_2$  content (Meehl et al. 2000a).

The atmospheric component, CCM3, is a spectral model with horizontal T42 truncation ( $\sim 2.8^\circ$  horizontal resolution). CCM3 has 18 layers in the vertical (3 in the planetary boundary layer) with the top layer centered at 4.8 mb. The integration time step ( $\Delta t$ ) for CCM3 is 20 min (1 h for radiation). The ocean component, NCOM, has  $2.4^\circ$  resolution in longitude and variable resolution in latitude, with smallest grid spacing of  $1.2^\circ$  at the equator and in the Arctic and largest spacing of  $2.3^\circ$  at midlatitudes. In the vertical, NCOM has 45 levels, with 4 equal depth levels in the upper 50 m and 25 levels in the upper kilometer of the ocean. The  $\Delta t$  is 30 min for NCOM. The land surface model, LSM, runs on the same grid as CCM3 with a time step of 20 min. The

sea-ice model runs on the ocean model grid. The  $\Delta t$  is 1 h for the sea-ice model.

The component models of the CSM were first run separately during a spinup period (Boville and Gent 1998), and then run in coupled mode with no anthropogenic forcing for 40 yr before the first model year analyzed here (corresponding to 1870). Four climate simulations were completed. These are 1) a 230-yr control run with trace gas concentrations appropriate for 1870, 2) a historical run for the period 1870–1998 using historical forcings of greenhouse gases and aerosols, 3) a twenty-first-century run for 1980–2099 under the BAU scenario, and 4) a twenty-first-century run for 2005–2099 under the STA550 scenario (before 2005 STA550 is identical to BAU).

The greenhouse gas concentrations and atmospheric sulfate ( $\text{SO}_4$ ) loadings for the historical run (1870–1998) were based on observations. Annual, global mean concentration histories to 1990 for  $\text{CO}_2$ ,  $\text{CH}_4$ , and  $\text{N}_2\text{O}$  were those employed by the Intergovernmental Panel on Climate Change (IPCC) in their Second Assessment Report (Kattenberg et al. 1996). To extend these, observed  $\text{CO}_2$  data through 1996 were obtained from C. D. Keeling and T. P. Whorf (1997, personal communication) and  $\text{CH}_4$  data through 1996 were obtained from Dlugokencky et al. (1998). These were then further extended using the gas cycle models of Wigley (1993) and Osborn and Wigley (1994) through to 2100 (see below) with smooth transitions at the end of the observed records. For  $\text{N}_2\text{O}$ , the IPCC IS92a projection was used from 1990 onward (Prather et al. 1996, Table 2.5b).

The greenhouse gases whose longwave radiative effects are included directly in the CCM3 are water vapor,  $\text{CO}_2$ ,  $\text{O}_3$ ,  $\text{CH}_4$ ,  $\text{N}_2\text{O}$ , CFC12, and CFC11 (the latter is scaled to account for other halocarbons; see Kiehl et al. 1999). Of these, only water vapor is entirely predicted within the model.  $\text{CO}_2$  is assumed to be well mixed through the entire atmosphere, with no seasonal cycle. For ozone, a seasonally varying, three-dimensional dataset is used (Kiehl et al. 1999). Over 1870–1990, the evolution of tropospheric and stratospheric ozone is determined using a synthesis of observed and (where observed data are absent) model-generated data (Kiehl et al. 1999). Stratospheric ozone was assumed to be constant up to 1970. After 1990, tropospheric ozone was held constant, while stratospheric ozone changes were predicted externally using the two-dimensional model of Garcia and Solomon (1994) driven by halocarbon projections consistent with the Montreal Protocol and its recent amendments and adjustments. The concentrations of  $\text{CH}_4$ ,  $\text{N}_2\text{O}$ , CFC11, and CFC12 were specified at the earth's surface uniformly with no seasonal cycles. Upper-level concentrations are determined by the CSM through vertical mixing, advection, and atmospheric chemistry as described in Boville et al. (2001). Chemical processes are parameterized using simple first-order models with seasonally varying, zonally symmetric loss frequencies obtained using the two-dimensional model

of Garcia and Solomon (1994). For  $\text{CH}_4$ , this produces a source of water vapor in the stratosphere that has a nonnegligible radiative effect.

Atmospheric sulfate loadings are prescribed in the historical run based on the results of Barth et al. (2000), Kiehl et al. (2000), and Rasch et al. (2000) for the mid-1980s. These three-dimensional loadings were scaled proportional to global  $\text{SO}_2$  emissions using the emission history of Öm et al. (1996), preserving the seasonal cycle of the mid-1980s. This is clearly a crude approximation, since the spatial pattern of  $\text{SO}_2$  emissions has changed radically over the twentieth century. Natural emissions of sulfur compounds are included, but assumed not to change with time. The natural global mean loading accounts for about 25% of the total loading in the mid-1980s. For the BAU and STA550 future projections, spatially and seasonally varying emissions of  $\text{SO}_2$  are prescribed and the model is run with interactive sulfur chemistry (Rasch et al. 2000) to define sulfate loadings and their changes. The  $\text{SO}_2$  emissions were determined using the MiniCAM integrated-assessment–energy-economics model of Edmonds et al. (1997, see below).

### 3. Development of the scenarios

The strategy behind the two greenhouse gas and sulfate scenarios for the twenty-first century was to have a “matched” pair, an existing-policies (ACACIA-BAU) scenario and a policy (STA550) scenario. Future anthropogenic emissions of greenhouse gases and sulfur dioxide are highly uncertain even under the BAU assumption (Alcamo et al. 1995). We therefore chose to use a BAU scenario similar to the IPCC IS92a scenario (Leggett et al. 1992), since this is roughly in the center of the spectrum of published possibilities. Internally consistent emissions for the two most important gases,  $\text{CO}_2$  and  $\text{SO}_2$ , were generated using the MiniCAM integrated-assessment/energy-economics model of Edmonds et al. (1997), driven by regionally specific assumptions with regard to population growth, economic growth, energy use per capita, technology developments, etc. We used values for these quantities that lie in the middle of the ranges of accepted values.

For  $\text{CO}_2$ , the resulting emissions are similar to those for IS92a, and the concentration projection differs from IS92a by, at most, 6 ppmv (i.e.,  $\sim 0.05 \text{ W m}^{-2}$ ). Our  $\text{CO}_2$  concentrations are slightly less than those in IS92a before around 2060, and slightly greater subsequently. By 2100, the difference drops to near zero. The  $\text{CO}_2$  concentrations in our scenario match observed values through 1996, and then increase at a slightly faster rate than seen in the 1990s reaching  $\sim 710$  ppmv by 2100 (Fig. 1). The 2100  $\text{CO}_2$  level represents an approximate doubling of the levels in the 1990s.

The reason for not simply using IS92a is because of the well-recognized problems with  $\text{SO}_2$  emissions in all IS92 scenarios (Alcamo et al. 1995, 281–282). For this

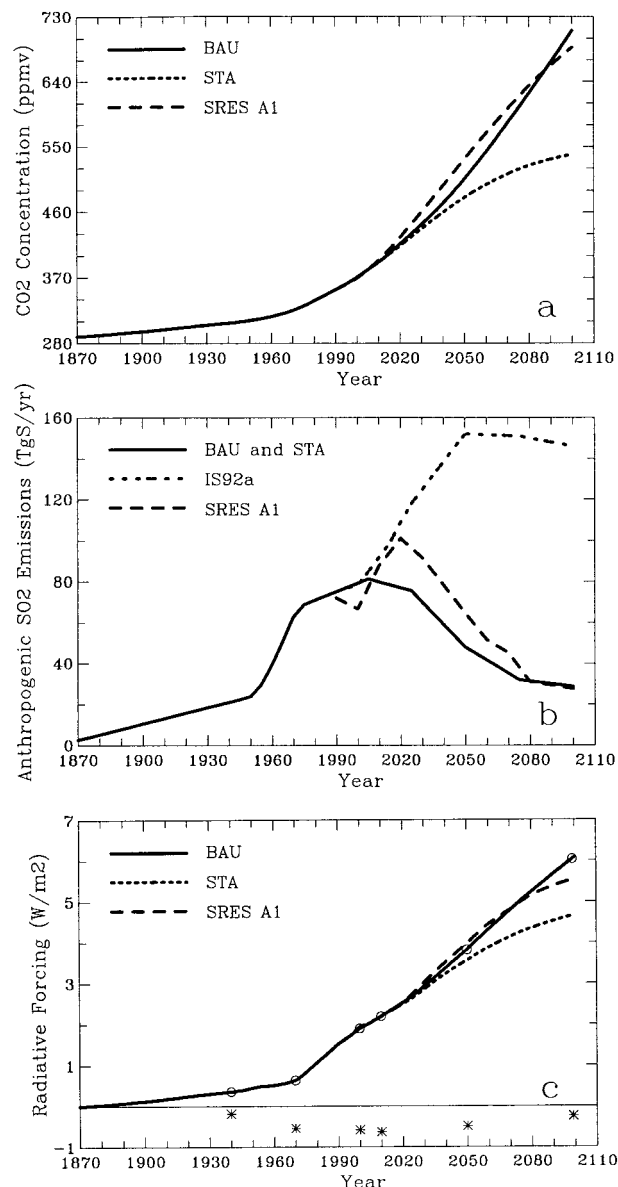


FIG. 1. (a) Global mean values of atmospheric  $\text{CO}_2$  concentrations (ppmv); (b) anthropogenic  $\text{SO}_2$  emissions ( $\text{Tg S yr}^{-1}$ ), and (c) radiative forcing at the tropopause by greenhouse gases and sulfate aerosols (curves) and by sulfate aerosols along (stars) from 1870 to 2100 ( $\text{W m}^{-2}$ ). Data before the 1990s are observations and thereafter are projected values under different scenarios. The forcing data in 1940, 1970, 2000, 2010, 2050, and 2100 (under the BAU scenario) were computed offline using CSM output. The fitted curves in (c) are estimates based on standard concentration-forcing relationships.

gas, the IS92a scenarios did not fully consider the effects of emission control policies to combat air pollution and acid rain that are likely to be implemented regardless of policies related to climate change. In the absence of such controls,  $\text{SO}_2$  emissions tend to increase as an economy grows, leading to a parallel increase in the environmental impacts of these emissions. At the same time, however, as economies grow, both the desire and

capability to control  $\text{SO}_2$  emissions increase. The  $\text{SO}_2$  emissions, therefore, are directly tied to economic levels. Given this, one would expect developing countries (China, India, etc.) to follow the pathway already trodden by North America, Europe, and other developed countries and to apply increasing controls on  $\text{SO}_2$  emissions in the future. The latest version of MiniCAM takes these effects into account (Smith et al. 2000). Thus, while the  $\text{CO}_2$  emissions used in our BAU scenario are similar to those in IS92a, our  $\text{SO}_2$  emissions differ radically from IS92a (see Fig. 1). Rather than increase by roughly 100% over the twenty-first century (as in IS92a), our  $\text{SO}_2$  emissions begin with a slight increase and then decline to less than half the present value by 2100 (Fig. 1). This radical change is entirely consistent with other recent work, which is epitomized by the new IPCC Special Report on Emissions Scenarios (SRES; for a brief description of the SRES scenarios, see Wigley 1999, p. 36). For comparison, Fig. 1 also shows  $\text{SO}_2$  emissions under a preliminary version of the SRES A1 scenario, which are qualitatively consistent with our own projection.

For  $\text{CH}_4$ , existing BAU emission scenarios (such as IS92a) provide concentration values for recent years that are too high relative to observations. We therefore chose a concentration scenario directly (i.e., without any prior specification of emissions) that matched observed concentrations (from Dlugokencky et al. 1998) through 1996 and stabilized at 2500 ppbv in 2100. This 2100 level is considerably lower than the 3616 ppbv reached for the IS92a scenario (Prather et al. 1996, Table 2.5a). Relative to IS92a, it represents a reduced radiative forcing of approximately  $0.3 \text{ W m}^{-2}$  in 2100.

For the other gases, we used the IS92a scenario for  $\text{N}_2\text{O}$ , and assume that halocarbons follow a preliminary version of the IPCC SRES A1 scenario. The scenario for halocarbons takes account of the Montreal Protocol and its recent amendments and adjustments, leading to substantially reduced concentrations of controlled gases (such as CFC11, CFC12, HCFC22, etc.) by 2100. In direct radiative forcing terms, these reductions are offset by increases in the concentrations of substitute gases (mainly HFCs) and (to a much lesser extent) increases in the concentrations of species not currently being controlled under the Montreal Protocol (such as the perfluorocarbons and  $\text{SF}_6$ ). In our simulations, halocarbons other than CFC11 and CFC12 are accounted for by scaling up the concentration of CFC11 to give the same total direct radiative forcing (see Kiehl et al. 1999).

For the  $\text{CO}_2$  stabilization (STA550) scenario, we made only one change. We assumed that atmospheric  $\text{CO}_2$  concentrations would stabilize at 550 ppmv in 2150 following a pathway similar to the WRE550 pathway (Wigley et al. 1996), as a result of implementation of certain  $\text{CO}_2$  stabilization policies. The  $\text{CO}_2$  concentrations under the STA550 scenario follow the BAU scenario to 2005, fall noticeably below those of the BAU scenario after  $\sim 2030$  and stabilize by 2150 ( $\sim 540$  ppmv



in 2100, see Fig. 1). Figure 1 also shows CO<sub>2</sub> concentrations and SO<sub>2</sub> emissions under the SRES A1 scenario, since a model run has also been completed for this case (cf. Figs. 17 and 24).

Figure 1c shows the global mean total radiative forcing (curves) at the tropopause by the greenhouse gases and sulfate aerosols and the forcing by sulfate aerosols alone (stars). It can be seen that the forcing curves generally follow those of the CO<sub>2</sub> concentrations, which is the dominant forcing agent. The mean total forcing increases almost linearly from zero in 1870 to 0.63 W m<sup>-2</sup> in 1970 and then rises to 6.1 (4.7) W m<sup>-2</sup> in 2100 under the BAU (STA550) scenario at a much higher rate (Fig. 1c). The maximum cooling by sulfate aerosols is about 0.63 W m<sup>-2</sup> around 2010.

#### 4. Twentieth-century climate

The performance of the CSM in simulating present climate has been evaluated extensively in a number of papers published in the June 1998 issue of *Journal of Climate*. In general, the atmospheric component (CCM3) of the CSM simulates the geographic and interannual variations of air temperatures, precipitation, humidity, and winds fairly well when observed sea surface temperature (SST) is used (Kiehl et al. 1998; Hack et al. 1998; Hurrell et al. 1998). The ocean component of the CSM simulates the ocean temperature, salinity, and circulation fields reasonably well when the observed atmospheric forcing is used (Gent et al. 1998). In coupled control runs, the simulated atmospheric and surface climates (including SST) are comparable to observations and stable without flux adjustments, but the surface (deep) ocean salinity has a negative (positive) bias and several aspects of the ocean circulation are unrealistic (e.g., the Antarctic Circumpolar Current is too strong, Boville and Gent 1998; Boville and Hurrell 1998). These biases have been greatly reduced in the version of CSM used here (Boville et al. 2001). The sea-ice cover in the CSM is also too extensive in the North Pacific and the subarctic North Atlantic Oceans (Weatherly et al. 1998), which induces excess positive feedback and comparatively large warming over these regions in the BAU and STA550 runs.

To provide some credibility for the model-simulated future climate changes discussed in the next section, we first compare the observed and CSM-simulated spatial patterns and seasonal and year-to-year variability of surface air temperature, precipitation, cloudiness, humidity, winds, synoptic storm activities, El Niño–Southern Oscillation (ENSO), and the North Atlantic oscillation (NAO) of the twentieth century. In the following, the periods of comparison were chosen based on the availability of observational data. When direct observations were not available, we used the National Centers for Environmental Prediction–National Center for Atmospheric Research (NCEP–NCAR) reanalysis data, which contain uncertainties (Kalnay et al. 1996).

##### a. Air temperature

Figure 2 shows the 1961–90 mean annual surface air temperature<sup>1</sup> simulated by the CSM and the CSM-minus-observed temperature difference. The main features of the temperature field, namely the meridional gradients, land–ocean differences, and tropical warm zones (see e.g., Jones et al. 1999) are captured reasonably well by the CSM. The CSM, however, has a cold bias of about 2°–6°C over Eurasia and Africa, and the differences are large (~4°–6°C) in the polar regions, where the observed climatology is less reliable (especially over the Antarctic) and the simulated temperature is sensitive to the sea-ice model used in the CSM (Weatherly et al. 1998). Other noticeable differences include warm biases (1°–2°C) over the subtropical oceans west of South America and Africa, and cold biases (2°–4°C) over the North Pacific and the subarctic North Atlantic, where sea-ice cover is too extensive in the CSM (Weatherly et al. 1998). The cold biases over land and warm biases over the subtropical oceans are related to the overestimate and underestimate of cloud amount over these areas, respectively (see Fig. 8 later).

The seasonal cycle of zonal mean surface air temperature in the CSM (not shown) is generally similar to the observed (e.g., Jones et al. 1999). The cold biases at northern latitudes and warm biases at southern latitudes vary little through the year, except over northern high latitudes, where the CSM-simulated winter and autumn temperatures are considerably (~5°–6°C) colder than observed. This results in a larger-than-observed seasonal cycle at northern high latitudes. The spatial patterns of year-to-year variations of surface air temperatures (Shea 1986) are also simulated reasonably well by the CSM (Fig. 3). However, the CSM underestimates the variability by about 20% over much of the globe, particularly over the low-latitude Atlantic and eastern Pacific (by ~40%). In contrast, it overestimates the variability by 20%–60% over the North Atlantic and northwestern Europe, the North Pacific, and the eastern Ross Sea due to strong sea-ice variability in the model (Weatherly et al. 1998). The CSM-simulated variability over Australia is also larger (by ~10%–20%) than observed.

The vertical structure (including the tropopause) of the CSM-simulated atmospheric temperature compares favorably overall with that of the NCEP–NCAR reanalysis (Fig. 4). However, the CSM produces slightly larger than observed meridional temperature gradients over mid- and high latitudes in the lower troposphere (mainly over the winter hemisphere). The simulated temperature around tropopause over the Tropics is also about 5°C colder than the reanalysis.

The observed changes of surface air temperature dur-

<sup>1</sup> Surface air temperature from the CSM is the air temperature at the reference height (2 m above all surfaces).

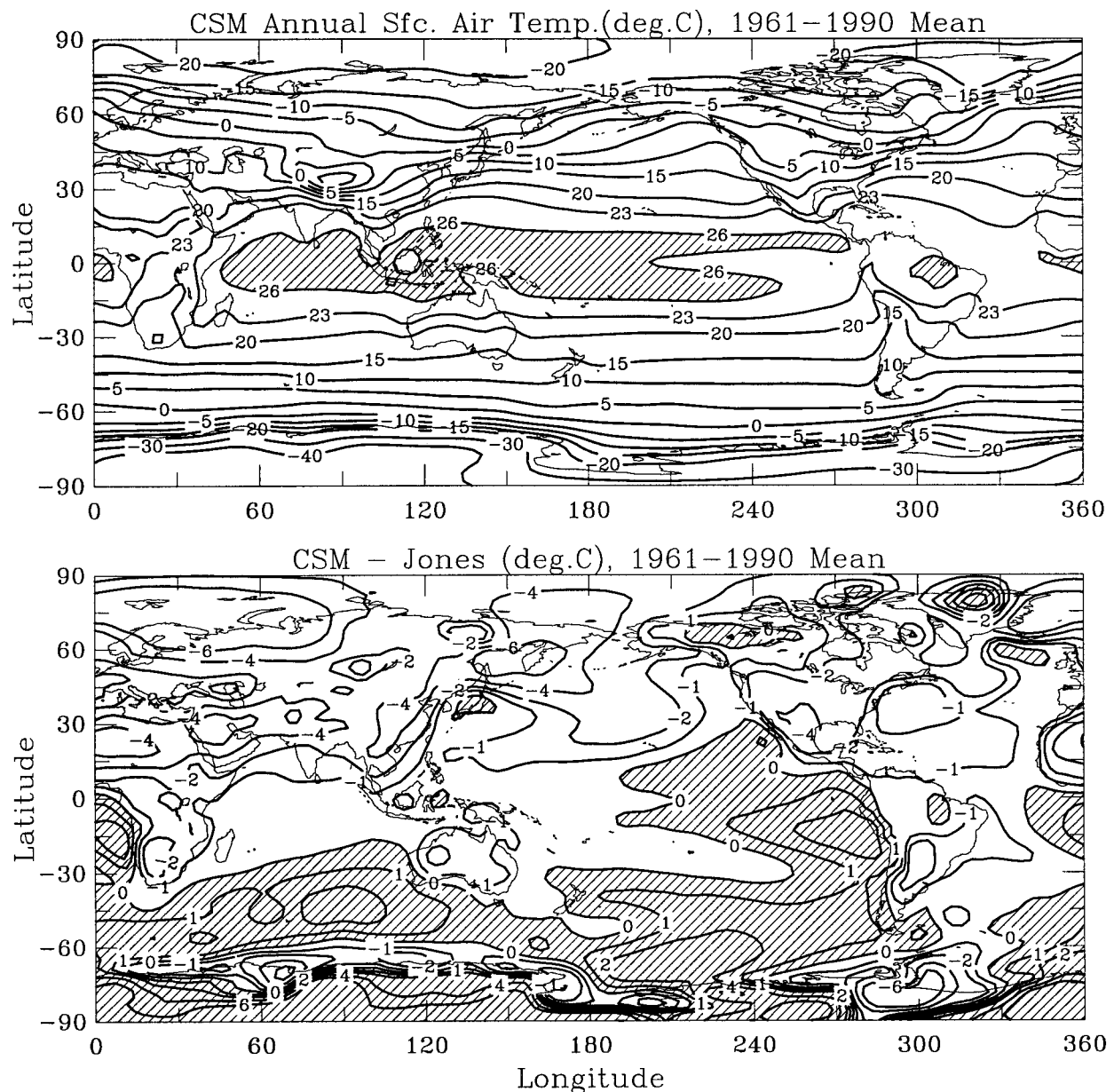


FIG. 2. Annual mean surface air temperature ( $^{\circ}\text{C}$ ) for 1961–90: (top) from the CSM and (bottom) for CSM minus Jones et al. (1999) difference.

ing the twentieth century are simulated reasonably well (Figs. 5 and 17 later), except for the observed rapid warming from the 1920s to the 1940s. This observed warming is substantially larger than expected from coupled GCMs (Santer et al. 1996, Fig. 8.3), implying that external forcing played an important role. Its absence in the CSM simulation may be partly due to our neglect of additional external forcings such as increases in solar irradiance (by  $\sim 1.5 \text{ W m}^{-2}$ , see e.g., Lockwood and Stamper 1999; Solanki and Fligge 1999) that are not included in the model simulation. The rapid warming since the 1970s, which is also well above the range of

internal variability expected from the control runs, is captured remarkably well by the CSM.

Figure 5 compares the CSM-simulated twentieth-century time series of zonal mean surface temperature with observations from Jones et al. (1999). The CSM captures the observed warming (largest over mid- and high latitudes) since the late 1970s. However, the simulated surface temperature from about  $50^{\circ}$  to  $70^{\circ}\text{N}$  is colder than the observed from the 1920s to the 1950s. This cold bias occurs primarily in winter and over the North Atlantic and western Europe, where surface temperatures are sensitive to the sea-ice cover off Green-

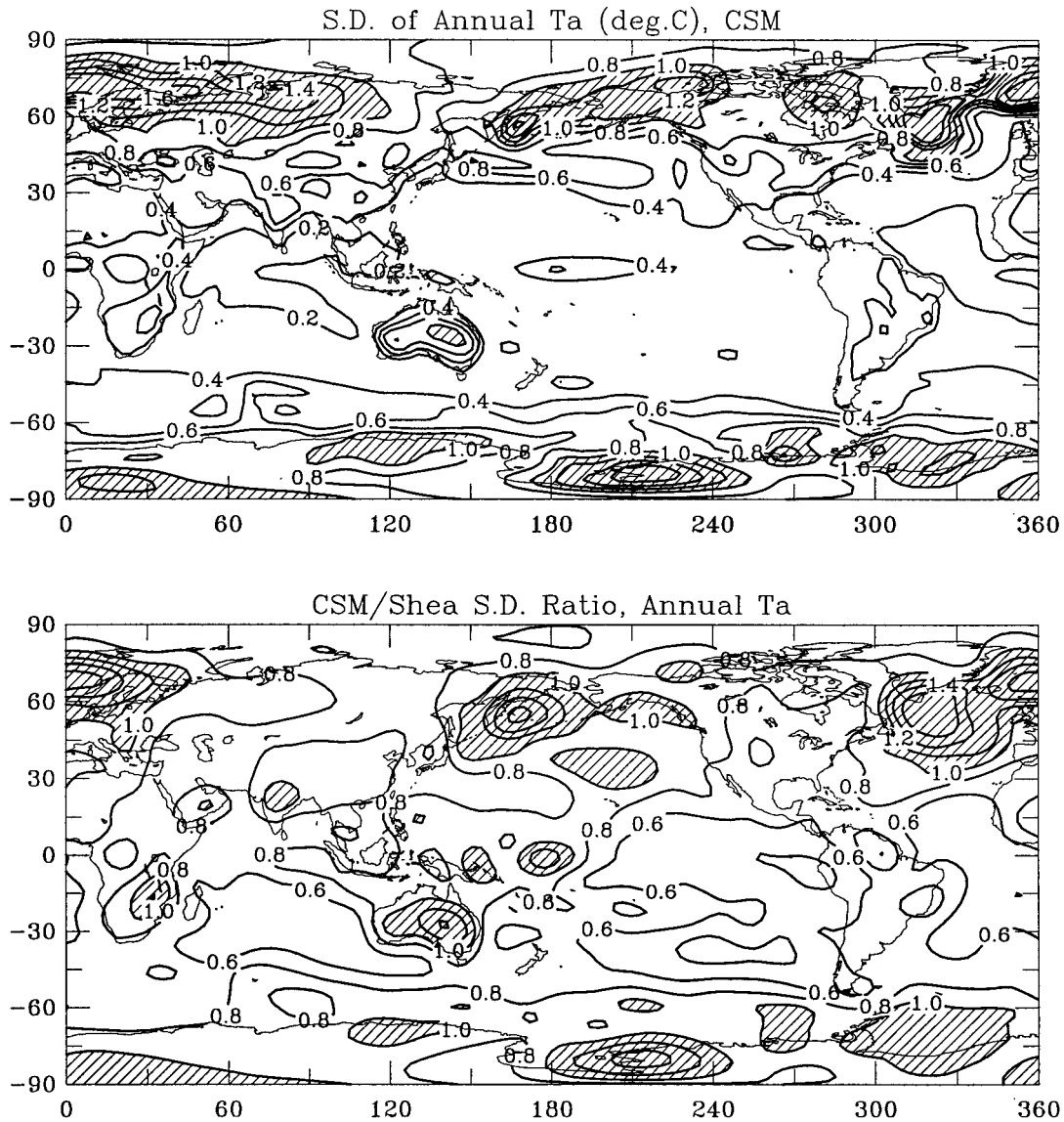


FIG. 3. Standard deviation of annual mean surface air temperature ( $^{\circ}\text{C}$ ) for 1950–79: (top) from the CSM and (bottom) for CSM/observed std dev ratio. Observations are from Shea (1986). Areas with values over 1.0 are hatched.

land. The simulated winter and spring sea-ice cover over the northern high latitudes was stable until the early 1970s when it started to shrink, particularly around Greenland. The melting of sea ice provides a strong positive feedback and contributes to the large warming of the 1980s and 1990s over the North Atlantic region in the model, which is not so obvious in the observations.

#### b. Precipitation, cloudiness, and humidity

Figure 6 compares the CSM-simulated 1979–98 mean annual precipitation rate (the global mean rate is  $2.99 \text{ mm day}^{-1}$ ) with that derived from rain gauge obser-

vations and satellite estimates (Xie and Arkin 1997; the global mean rate is  $2.68 \text{ mm day}^{-1}$ ). It can be seen that the large-scale patterns are simulated well, especially considering that present precipitation climatologies can differ by 10%–100% (with largest differences over the oceans and mountainous regions; Dai 1996). The major discrepancies include wet biases over the central and eastern tropical Pacific south of the equator; tropical Africa; high terrain such as the Himalaya, the Rocky Mountains and the Andes; and the subtropical oceans west of South America. The CSM also has a dry bias over southern Asia.

Plots of the seasonal cycle of zonal mean precipitation (not shown) reveal that the CSM approximately repro-

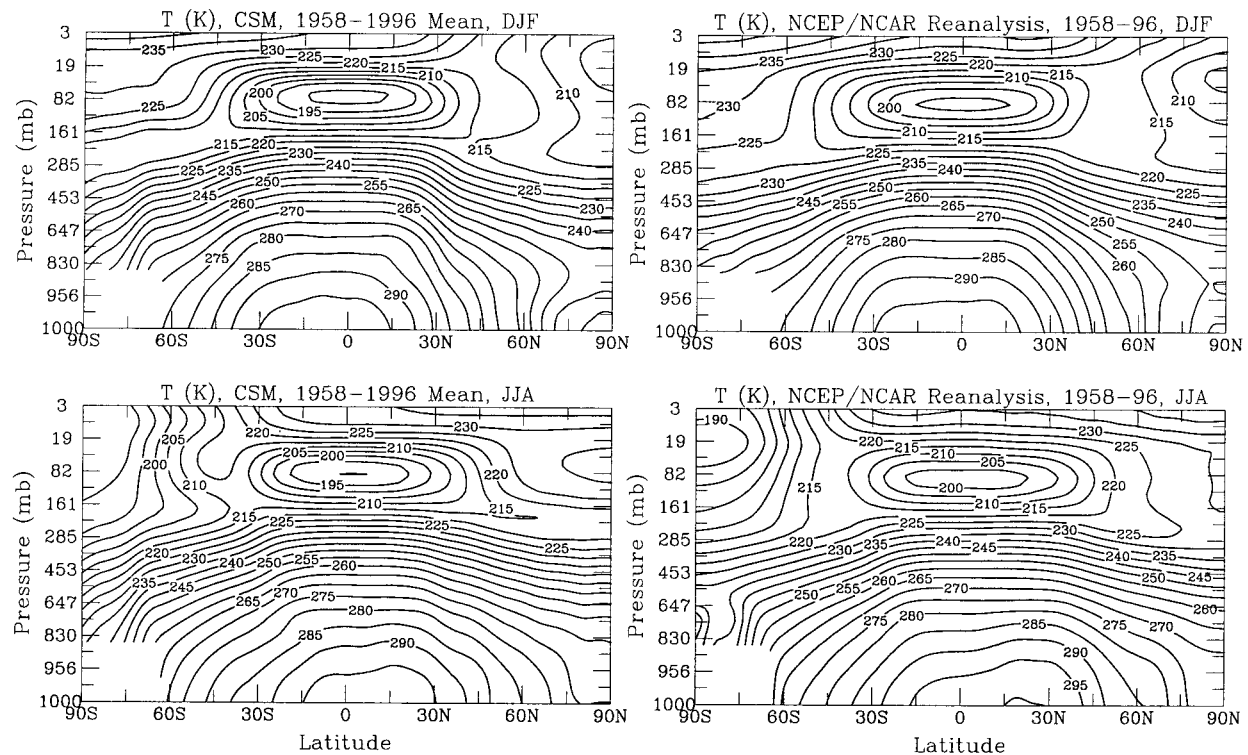


FIG. 4. Latitude–height distribution of zonal mean air temperature (K) for 1958–96 for (top) Dec–Feb (DJF) and (bottom) Jun–Aug (JJA) from (left) the CSM and (right) the NCEP–NCAR reanalysis (Kalnay et al. 1996).

duces the meridional movement of the tropical rain band, and the seasonal cycle of precipitation over mid- and high latitudes. In general, however, the CSM tends to produce more than observed precipitation during winter and spring over low and midlatitudes.

Figure 7 shows that the year-to-year variations of annual precipitation in the CSM are comparable with those in observations (Xie and Arkin 1997) over much of the globe. Over the eastern Pacific south of the equator and the subtropical oceans west of South America, North America, and Africa, the CSM-simulated precipitation variability is larger than that in the Xie–Arkin climatology. This bias exists in both winter and summer months. However, precipitation observations have large uncertainties over these oceanic regions.

The CSM-simulated twentieth-century time series of zonal mean precipitation (not shown) over northern mid- and high-latitude land areas exhibit variations comparable with observations from Dai et al. (1997a). For example, there is a weak increasing trend (superimposed on top of the large interannual variations) of precipitation over these latitudes during the twentieth century in both the observations and the CSM. However, the CSM failed to capture the large observed decadal variations in the Tropics, such as the large negative anomalies during the 1980s and 1990s and at the beginning of the century. These decadal changes over tropical land areas are largely caused by the low-frequency variation

in ENSO (Trenberth and Hoar 1996; Dai et al. 1997a). Decadal variations in ENSO are not well simulated by the CSM (Meehl and Arblaster 1998).

Compared with satellite observations (Fig. 8), the total cloud cover (derived using random overlap) in the CSM has a positive bias of up to 30% (of the sky cover) over land areas and the eastern equatorial Pacific, and a negative bias of 10%–40% over the subtropical and midlatitude oceans. In particular, subtropical marine stratus clouds are underestimated by 20%–30% in the CSM. These cloudiness biases are reflected in the cloud forcing of the CSM (Kiehl et al. 1998).

The CSM-simulated latitude–height distributions of zonal mean specific humidity are comparable with those from the NCEP–NCAR reanalysis (Kalnay et al. 1996), although the meridional gradients over mid- and high latitudes in the lower troposphere are larger in the CSM than in the reanalysis (Fig. 9). This bias is related to the similar problem in air temperature (Fig. 4). Observations of specific humidity over the polar regions and the upper troposphere are less reliable. The differences between the CSM and the reanalysis over these areas should therefore be interpreted cautiously.

### c. Atmospheric circulation

The maps of monthly mean sea level pressure (SLP) in the CSM (not shown here; see, e.g., Boville and Hur-



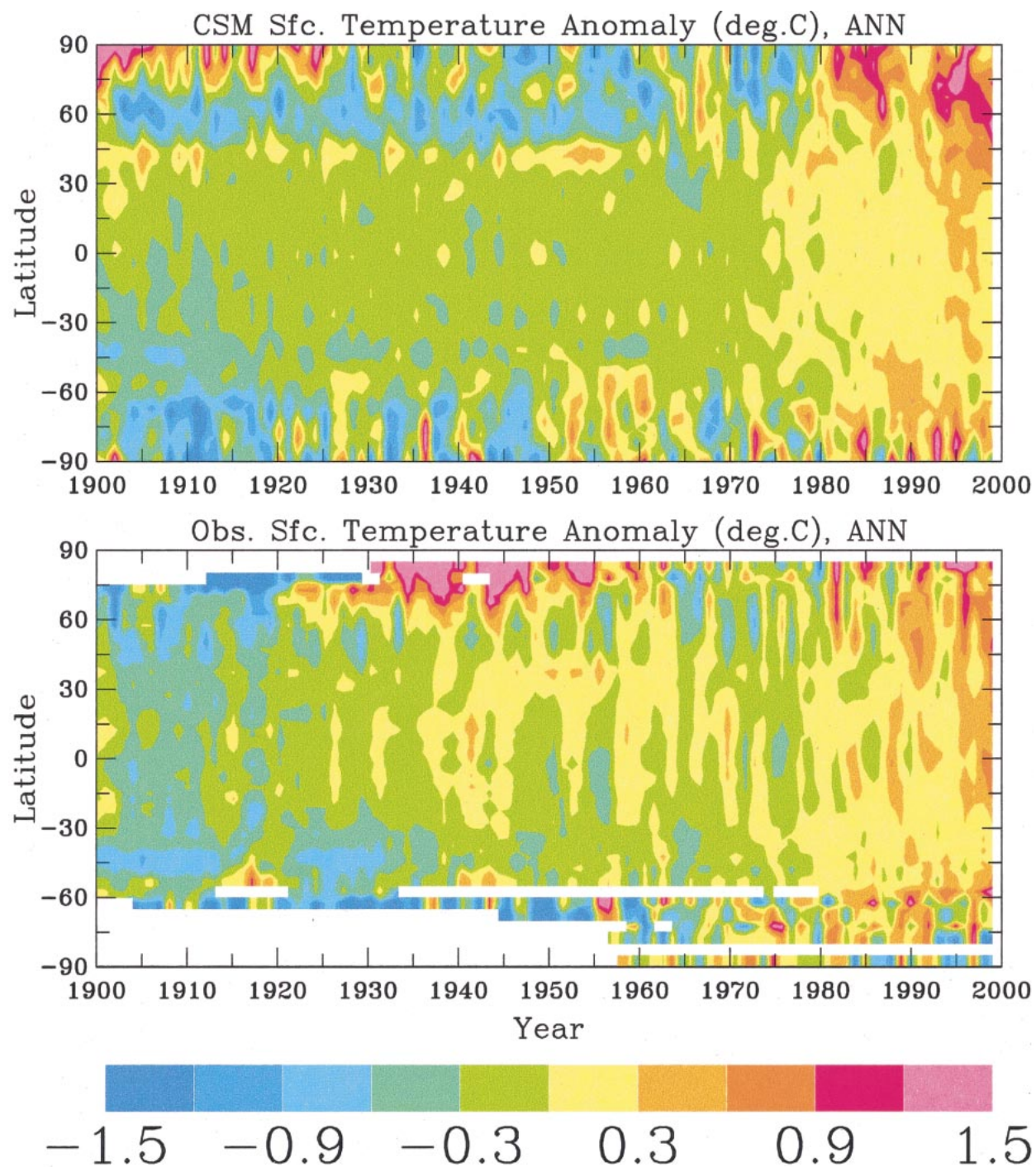


FIG. 5. Zonal mean annual surface temperature anomalies ( $^{\circ}\text{C}$ , relative to the 1961–90 mean) from 1900 to 1998 (top) from the CSM historical run and (bottom) from observations (from Jones et al. 1999). The surface temperature in this figure is surface air temperature (at 2 m above the ground) over land and sea surface temperature over ocean.

rell 1998) are similar to those from the NCEP–NCAR reanalysis. A more challenging task for the model is to correctly simulate the year-to-year variability of SLP. Figure 10 compares the December–February (DJF) and June–August (JJA) mean standard deviations of monthly

mean SLP from the CSM with those of the NCEP–NCAR reanalysis. It can be seen that the SLP variability is simulated well by the CSM. For example, the high-variability centers over the North Pacific and the North Atlantic during winter are captured well, although the

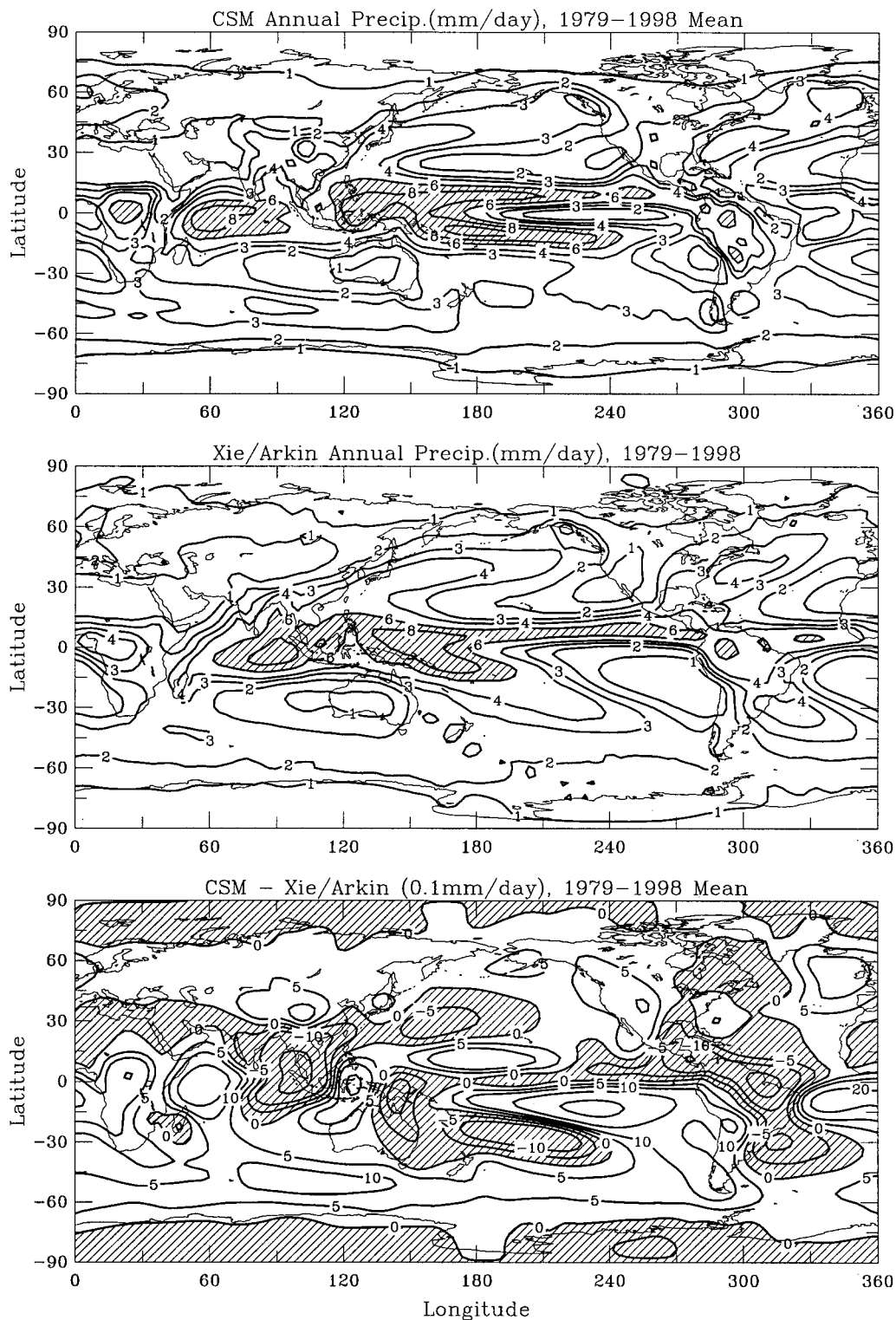


FIG. 6. (top) Annual mean precipitation ( $\text{mm day}^{-1}$ ) averaged over 1979-98 from the CSM and (middle) from Xie and Arkin (1997); and (bottom) the difference  $\times 10$  (i.e., in units of  $0.1 \text{ mm day}^{-1}$ ) between the two. Hatched areas indicate values exceeding  $6.0 \text{ mm day}^{-1}$  in the top and middle and below zero in the bottom.

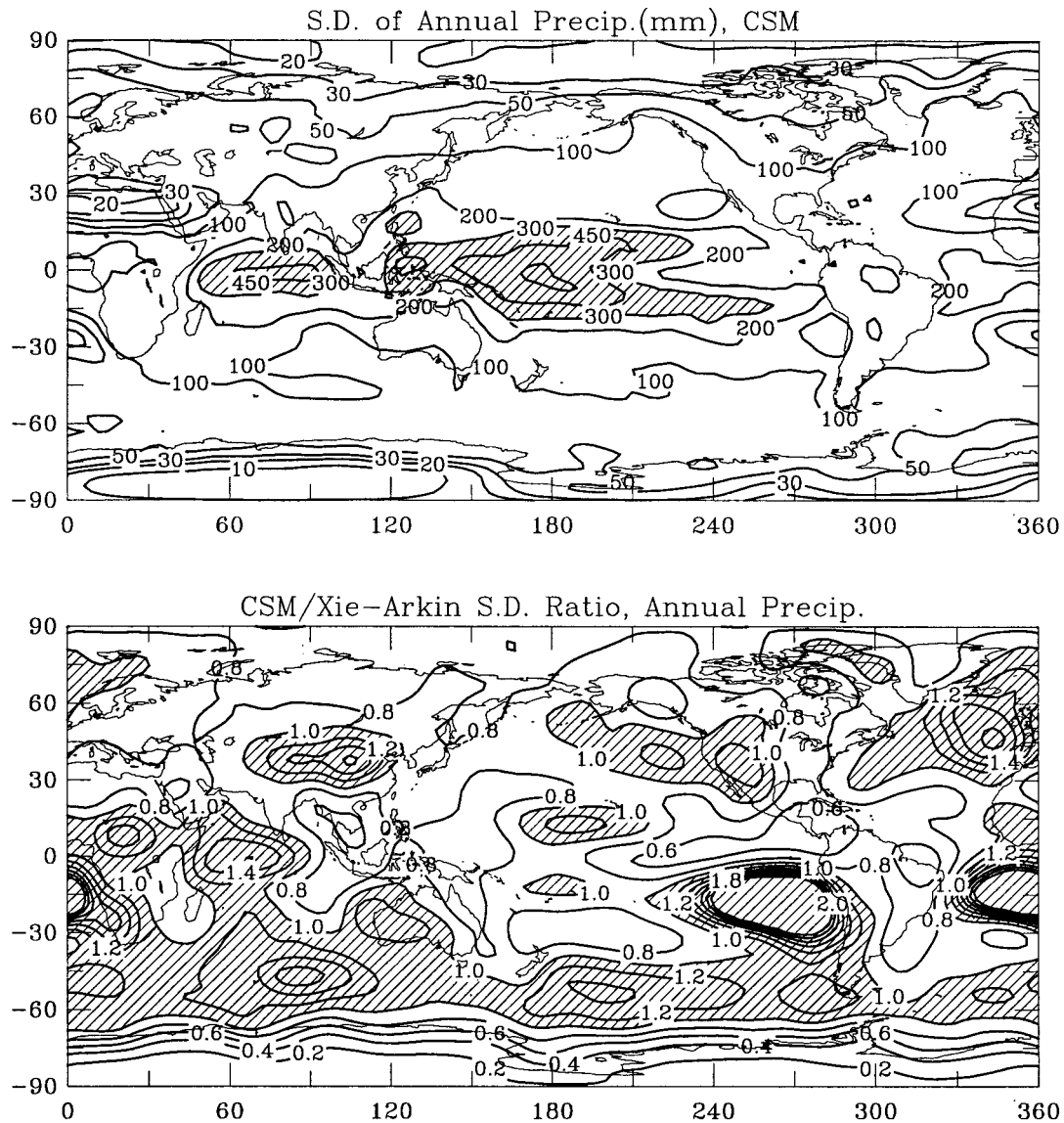


FIG. 7. Standard deviation of annual precipitation (mm) for 1979–98: (top) from the CSM; and (bottom) for CSM/observed std dev ratio. Observations are from Xie and Arkin (1997). Hatched areas indicate values exceeding 300 mm yr<sup>-1</sup> in the top and 1.0 in the bottom.

center over the North Atlantic is stronger and farther south than in the reanalysis. This bias results primarily from overestimated interannual variations in the CSM since multiyear-to-decadal variations are comparable to observations (cf. Fig. 16 later). The DJF to JJA difference in the variability is also well simulated.

On the timescales of synoptic systems or storms (2–8 days), the CSM simulates both the strength and location of the winter storm tracks remarkably well over northern mid- and high latitudes, except over Greenland, where the reanalysis is less reliable (Fig. 11). Storm activity over the Antarctic Circumpolar Current is also well simulated for both DJF (Fig. 11) and JJA (not shown).

Within the troposphere and the lower stratosphere,

the mean zonal winds are simulated reasonably well by the CSM (Fig. 12). However, the simulated subtropical jets are stronger (by ~20%) than the NCEP–NCAR reanalysis. The core locations of the simulated subtropical jets over the Southern Hemisphere are also higher (by ~40 mb) than in the reanalysis. Similar plots for meridional winds (not shown) also revealed broad agreements between the CSM and the reanalysis. This agreement is also indicated by the mean meridional streamfunction (Fig. 13) derived by integrating meridional winds vertically. However, Fig. 13 shows that the Hadley cell in the CSM is too strong compared with the NCEP–NCAR reanalysis, especially in the mid- and lower troposphere. On the other hand, the Hadley cell



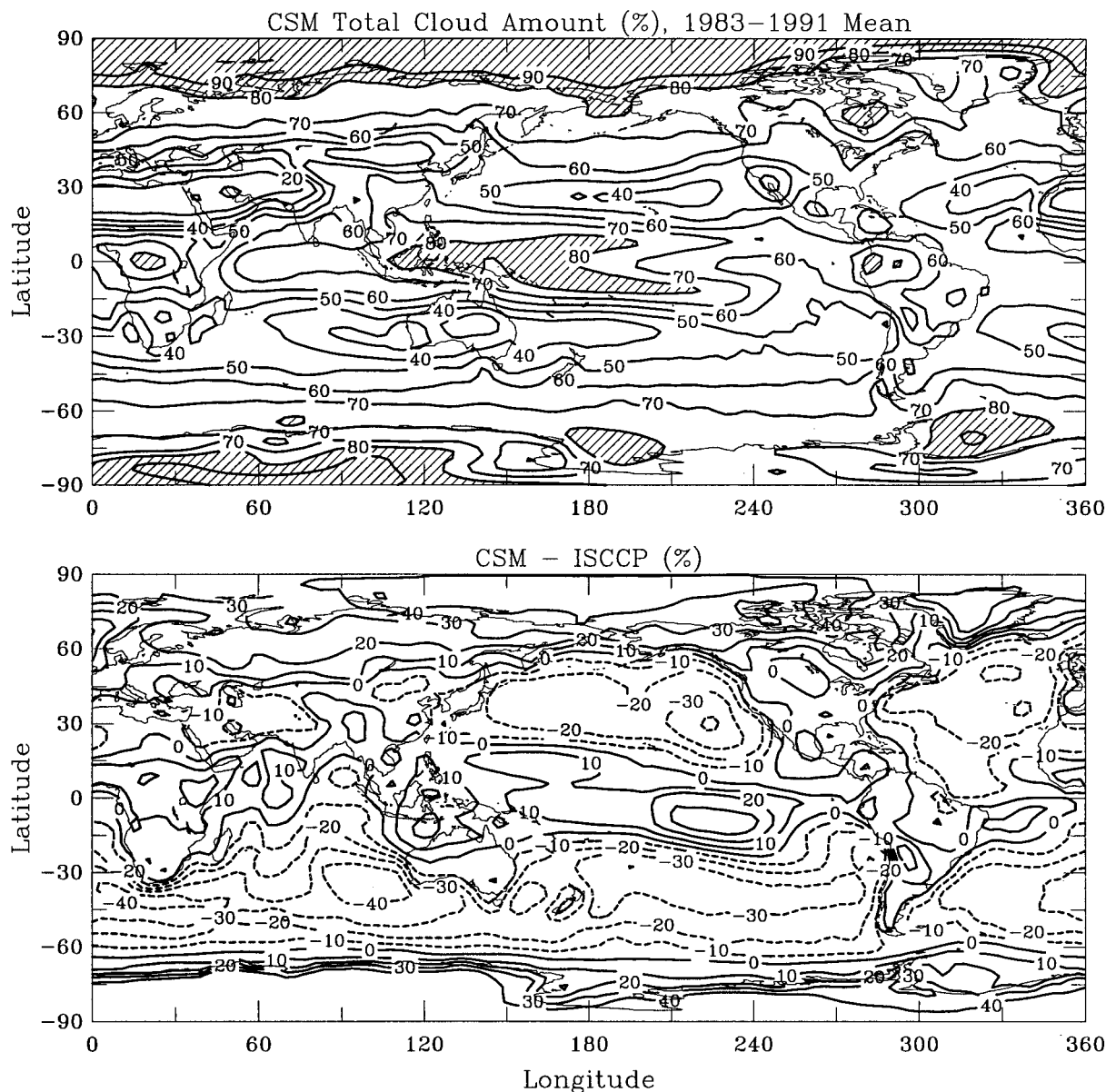


FIG. 8. Annual mean total cloud cover (% of the sky) averaged over 1983–1991: (top) from the CSM; and (bottom) for CSM minus ISCCP (Rossow and Schiffer 1991) difference. Values over 80% are hatched in the top. Negative values are in dashed curves in the bottom.

in the NCEP–NCAR reanalysis is about 10%–15% weaker than in the European Centre for Medium-Range Weather Forecasts reanalysis (Trenberth et al. 2000).

Zonal mean vertical motion in the troposphere is simulated well by the CSM (Fig. 14). In particular, the Hadley cell over both hemispheres and its seasonal variation [with equatorial convection moving into the summer hemisphere while subtropical subsidence (positive  $\omega$ ) strengthens in the winter hemisphere] are reproduced reasonably well by the CSM given its relatively coarse latitudinal resolution of  $\sim 2.8^\circ$ . Noticeable differences include stronger ascent in the Tropics (due to greater

penetration of moist convection, cf. Fig. 9) and weaker DJF subsidence in the lower troposphere over  $65^\circ$ – $83^\circ$ N in the CSM compared with the NCEP–NCAR reanalysis. [Note that the reanalysis has a higher latitudinal resolution of  $\sim 1.9^\circ$  (T63).]

#### d. ENSO and NAO simulations

The teleconnection patterns of atmospheric circulation, such as those associated with ENSO and the NAO, have large impacts on global and regional climate (e.g., Hurrell 1995; Dai et al. 1997a). Meehl and Arblaster



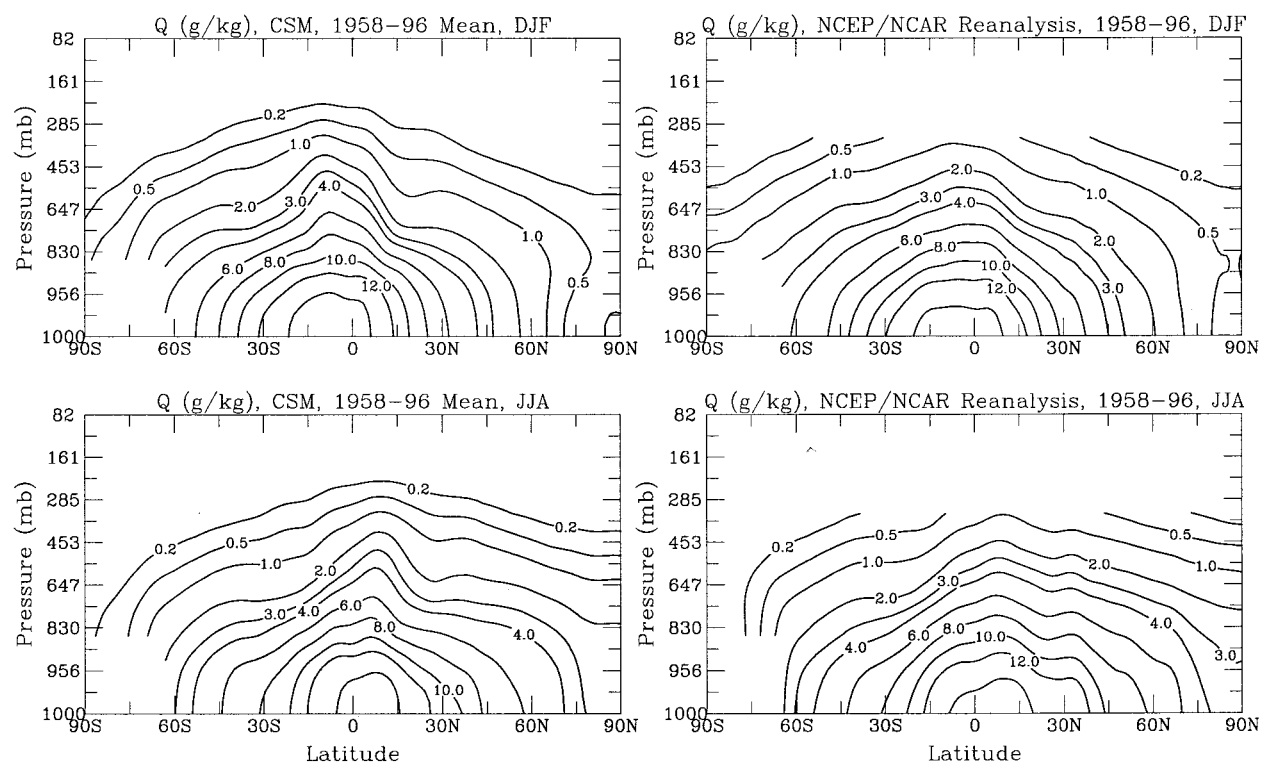


FIG. 9. (top) Latitude–height distribution of zonal mean DJF and (bottom) JJA specific humidity ( $\text{g kg}^{-1}$ ) for 1958–96 from (left) the CSM and (right) the NCEP–NCAR reanalysis.

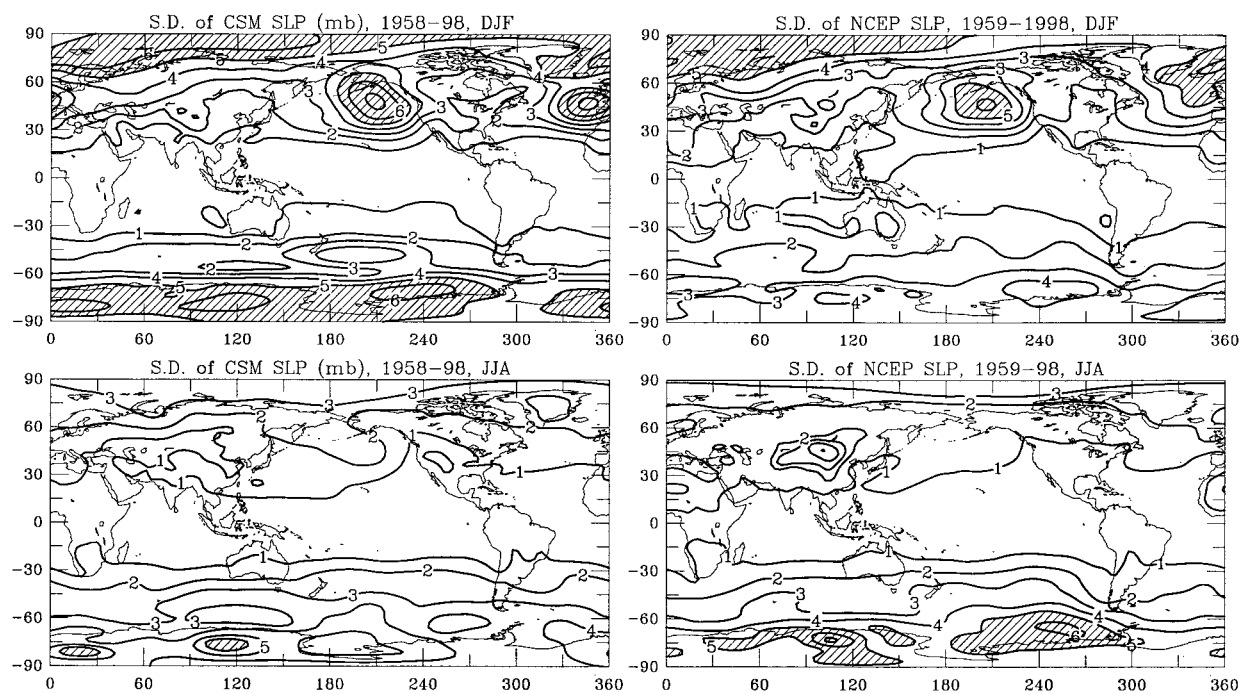


FIG. 10. (top) DJF and (bottom) JJA mean standard deviation (mb) of monthly SLP for 1958–98 from (left) the CSM and (right) the NCEP–NCAR reanalysis.

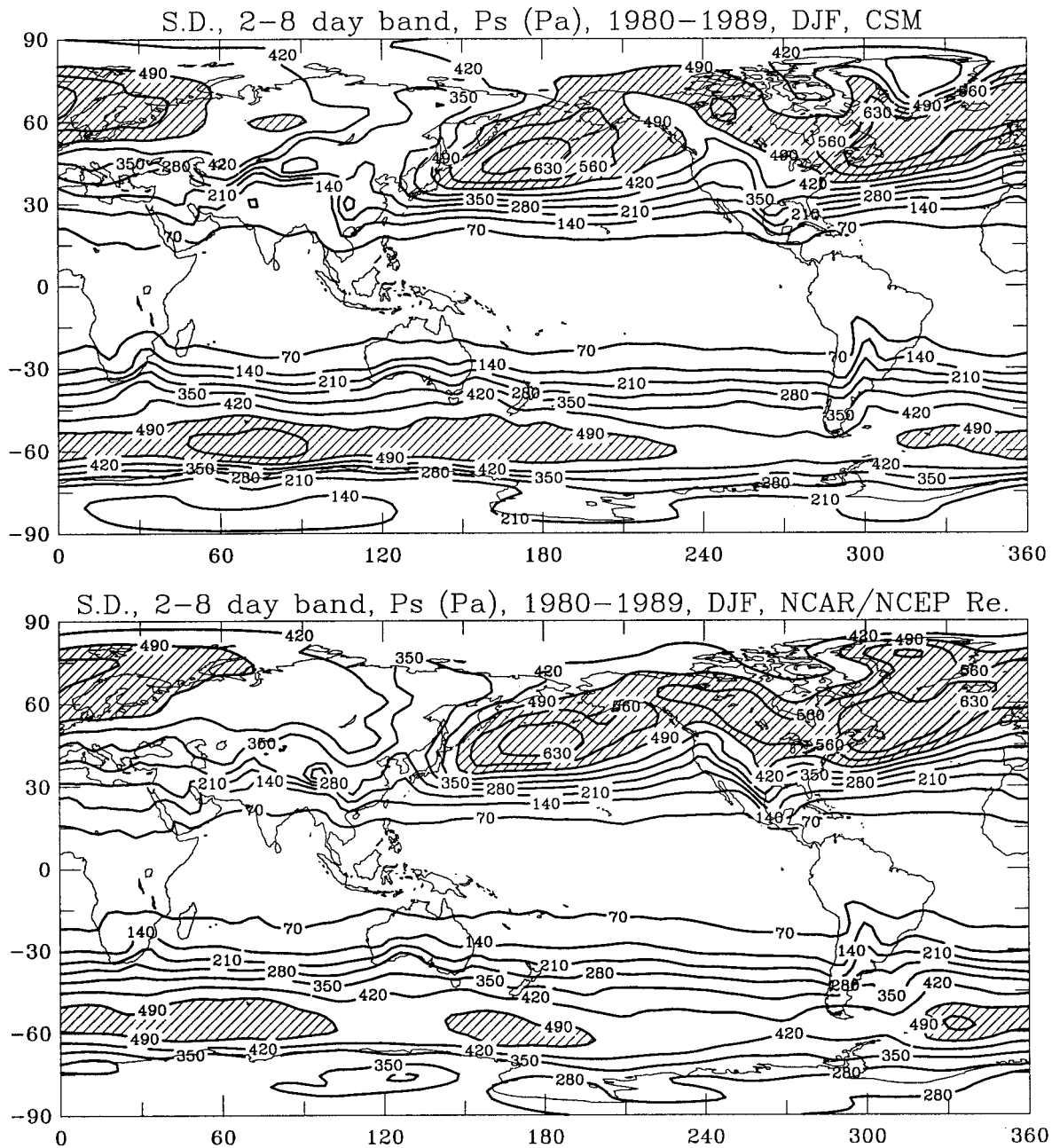


FIG. 11. DJF mean standard deviation (Pa) of band-passed 2–8-day variations of surface pressure for 1980–89 from (top) the CSM and (bottom) the NCEP–NCAR reanalysis. Areas with values exceeding 490 Pa are hatched.

(1998) show that the CSM simulates the interannual variability in the equatorial eastern Pacific SSTs with a reduced amplitude ( $\sim 60\%$  of observed), a common feature of many global coupled models (partly due to coarse model resolution). These authors also show that, in spite of this reduced amplitude, the CSM qualitatively reproduces the major spatial patterns in SLP and SST fields associated with the Southern Oscillation.

Figure 15 compares the first EOF of CSM-simulated and observed (Dai and Wigley 2000) annual precipi-

tation over the 1900–98 period. It can be seen that the CSM reproduces the broad patterns of ENSO-induced precipitation anomalies over low and midlatitudes, while the simulated EOF exhibits large variations around the ENSO timescales ( $2\text{--}7\text{ yr}^2$ ). The ENSO-like

<sup>2</sup> Note that the model simulation is only one random realization from a universe of possibilities. As such, there is no reason to expect it to follow the observations, especially on short timescales.

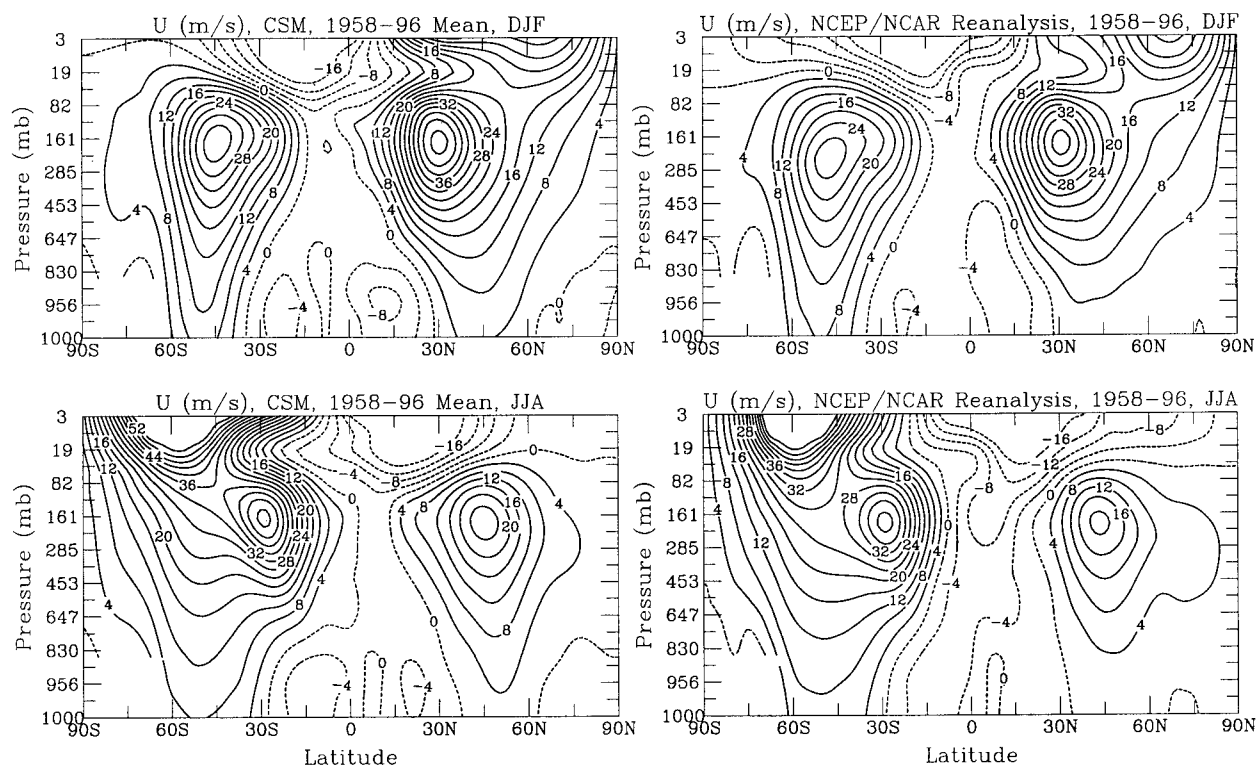


FIG. 12. Same as Fig. 9, but for the zonal wind component ( $\text{m s}^{-1}$ ). Negative values indicate easterly winds.

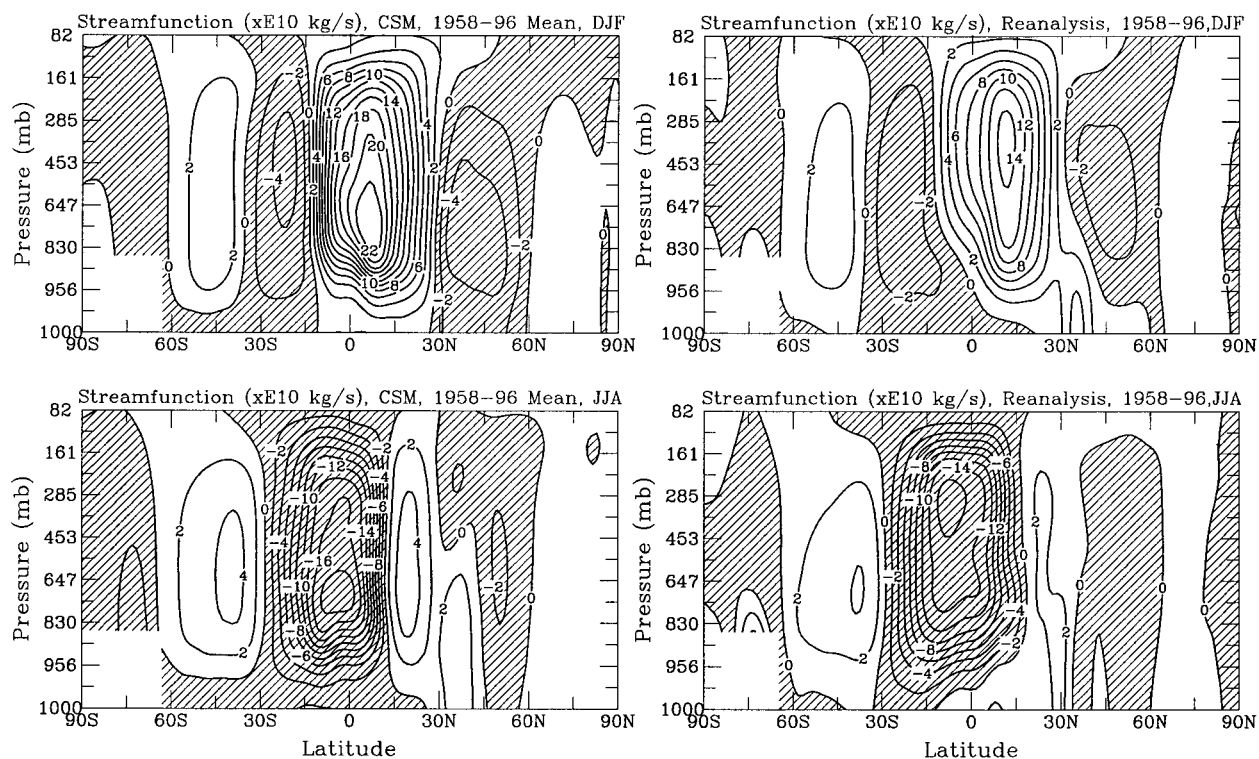


FIG. 13. Same as Fig. 9, but for mean meridional streamfunction ( $10^{10} \text{ kg s}^{-1}$ ) derived by vertically integrating the zonal mean meridional wind. Hatched areas indicate negative values.

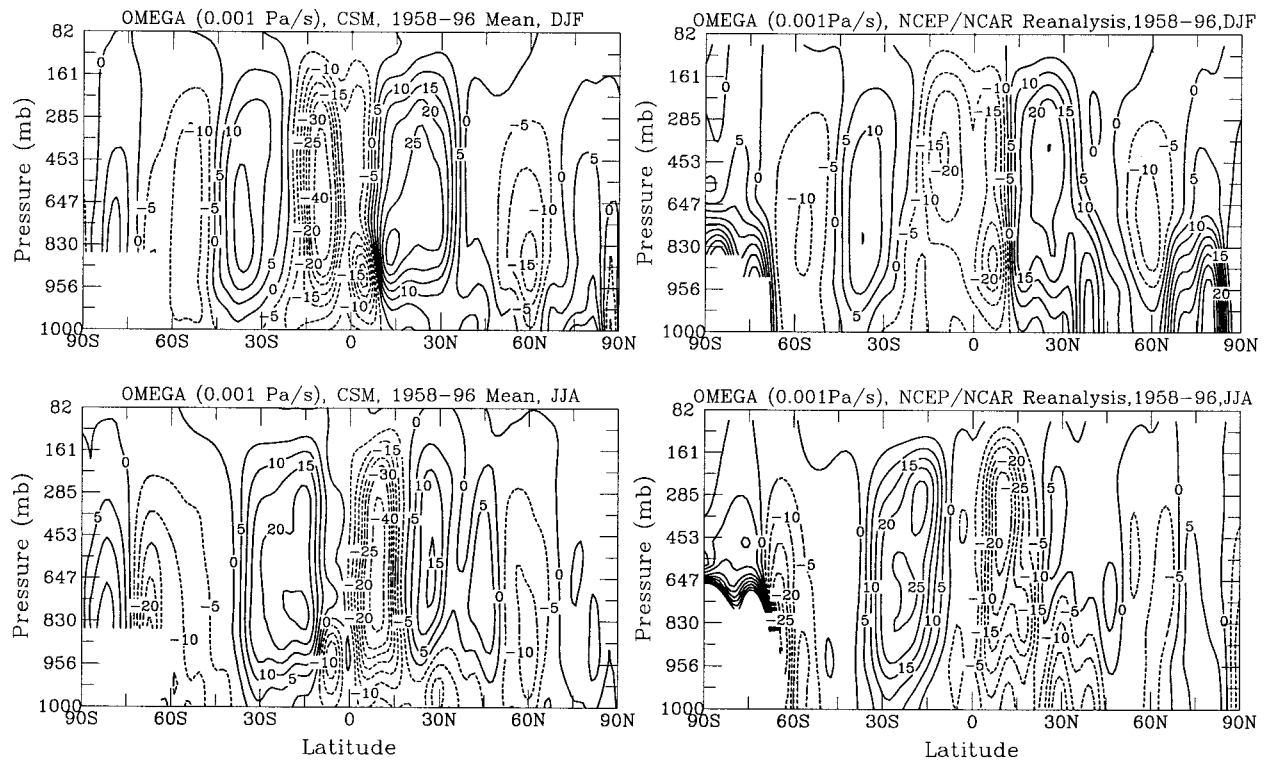


FIG. 14. Same as Fig. 9, but for vertical pressure-velocity  $\omega$  ( $10^{-3} \text{ Pa s}^{-1}$ ). Note that upward motion has negative  $\omega$ , which is in dashed curves.

precipitation mode in the CSM explains about 5.1% of the total variance, comparable with 5.6% for observations. There are, however, a number of differences in the simulated and observed ENSO modes. For example, the dry anomalies during El Niños are too small over eastern Australia and too large over the North Pacific and Alaska, while wet anomalies are too small over the equatorial eastern Pacific. The CSM also fails to capture the ENSO-induced precipitation anomalies over southern Africa.

The leading modes of variability of the extratropical circulation in both hemispheres are characterized by a multiyear oscillation that has opposite phases between the polar and midlatitude regions and accounts for about one-quarter of the total variance in sea level pressure and other fields (Thompson and Wallace 1998). Figure 16 compares the first EOF of CSM-simulated DJF SLP for the twentieth century with that of observed SLP from Trenberth and Paolino (1980 and updates) over the  $20^{\circ}$ – $90^{\circ}$ N region. It can be seen that the CSM reproduces the temporal and spatial variability of the observed mode fairly well. In the CSM, however, the simulated mode is stronger and explains a higher percentage of variance than the observed mode (38% vs 24%). The CSM also reproduces the annular mode of SLP variability over the extratropics of the Southern Hemisphere, with a slightly larger percentage of explained

variance than in the NCEP–NCAR reanalysis (not shown).

In summary, the CSM simulates the spatial and temporal variations of the twentieth-century climate reasonably well without surface flux adjustments. There are, however, significant biases that need to be addressed through future improvements of the model. The major biases include 1) a cold bias in surface air temperature over land areas, 2) overestimates of cloud amount (by 10%–30%) over land areas, 3) underestimates of cloud amount over the marine stratus regions west of North and South America and Africa, 4) underestimated variability of equatorial Pacific SSTs (Meehl and Arblaster 1998) and overestimated the South Pacific convergence zone precipitation, 5) a cold bias in the simulated surface air temperature at  $50^{\circ}$ – $70^{\circ}$ N from the 1920s to the 1940s (which may be due to additional external forcings such as changes in solar irradiance), and 6) a negative (positive) bias in surface (deep) ocean salinity (Boville and Gent 1998; Boville et al. 2001), and excess sea ice in the North Pacific and the subarctic North Atlantic Oceans (Weatherly et al. 1998).

Some of these problems are likely to be related. For example, the excessive cloudiness over land can block sunlight and contribute to the cold bias in surface temperature over land. Detailed diagnostic analyses of these problems are beyond the scope of this study. The sys-



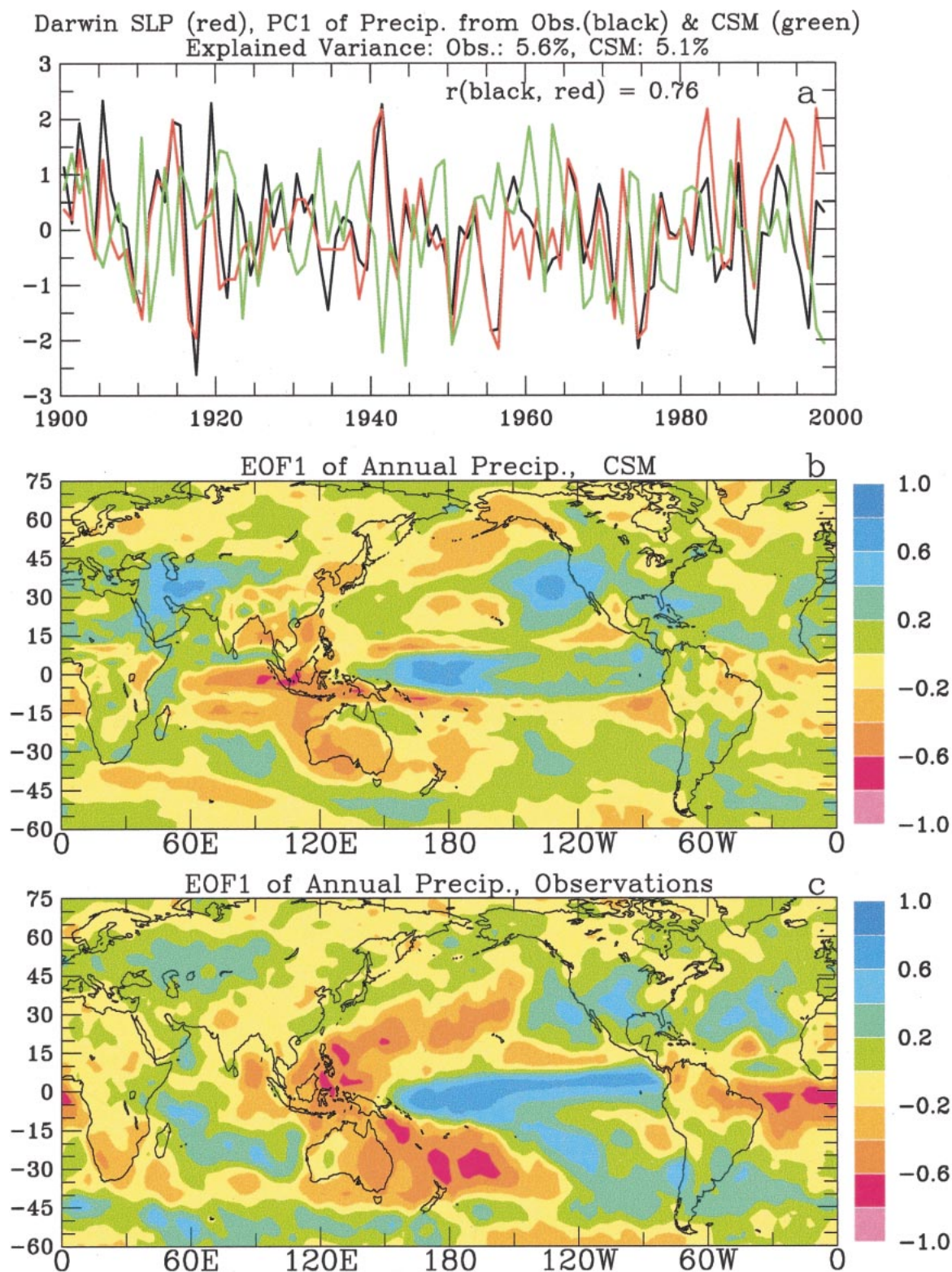


FIG. 15. (a) Temporal coefficients of the first EOF of annual precipitation from observations (Dai and Wigley 2000; black line) and the CSM (green line). Also shown (red line) is the normalized Darwin SLP as an ENSO indicator. Model values superimposed on observations do not imply predictability (because they are two random realizations) but simply illustrate relative amplitudes and timescales of variability. (b) Spatial pattern of the first EOF of annual precipitation from the CSM historical run. The values are normalized to represent the correlation coefficient between the EOF amplitude and the precipitation anomaly at each grid box. (c) Same as (b), but from observations (Dai and Wigley 2000).

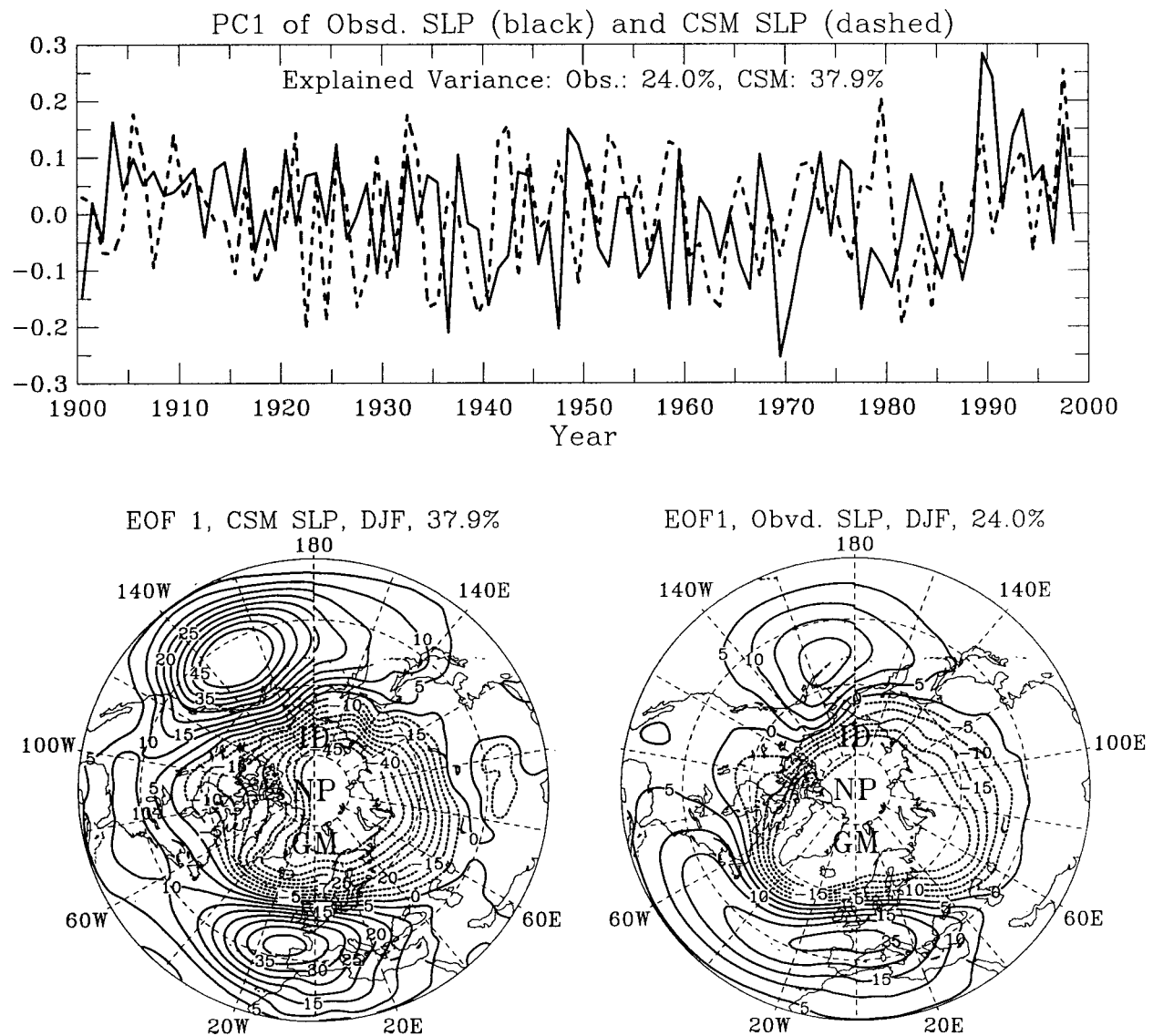


FIG. 16. (top) Amplitude time series for the first EOF of DJF SLP north of  $20^{\circ}\text{N}$  from observations (Trenberth and Paolino 1980; black line) and the CSM (dashed line). (bottom) Spatial pattern of the first EOF of DJF SLP from (left) the CSM historical run and (right) the observations. Negative contours are dashed. SLP data were not normalized in the EOF analysis.

tematic biases in the CSM may affect the simulated climate responses to future anthropogenic forcing (e.g., too much sea-ice feedback over the North Pacific and North Atlantic) and increase the uncertainties of the simulated changes.

## 5. Twenty-first-century climates

### a. Temperature changes

Figure 17 shows the smoothed global mean surface air temperature anomalies from various CSM simulations and compares them with the instrumental record (Nicholls et al. 1996 and updates). It can be seen that

the warming trend since the 1970s ( $\sim 0.18^{\circ}\text{C decade}^{-1}$ ) continues into the twenty-first century. Even though noticeable differences of  $\text{CO}_2$  concentrations are evident by the 2030s (Fig. 1), it is not until the 2050s that the  $\text{CO}_2$  stabilization scenario (STA550) starts to diverge from the BAU scenario with a lower warming rate ( $\sim 0.12^{\circ}\text{C decade}^{-1}$ ). From 1990 to 2099, the global mean temperature increases by about  $1.9^{\circ}\text{C}$  in the BAU case (the atmospheric  $\text{CO}_2$  concentration approximately doubles during the period), and by about  $1.5^{\circ}\text{C}$  in the STA550 case (in which case, the  $\text{CO}_2$  increase over 1990–2099 is roughly half of that for the BAU case). The IPCC SRES scenario A1 yields a global warming



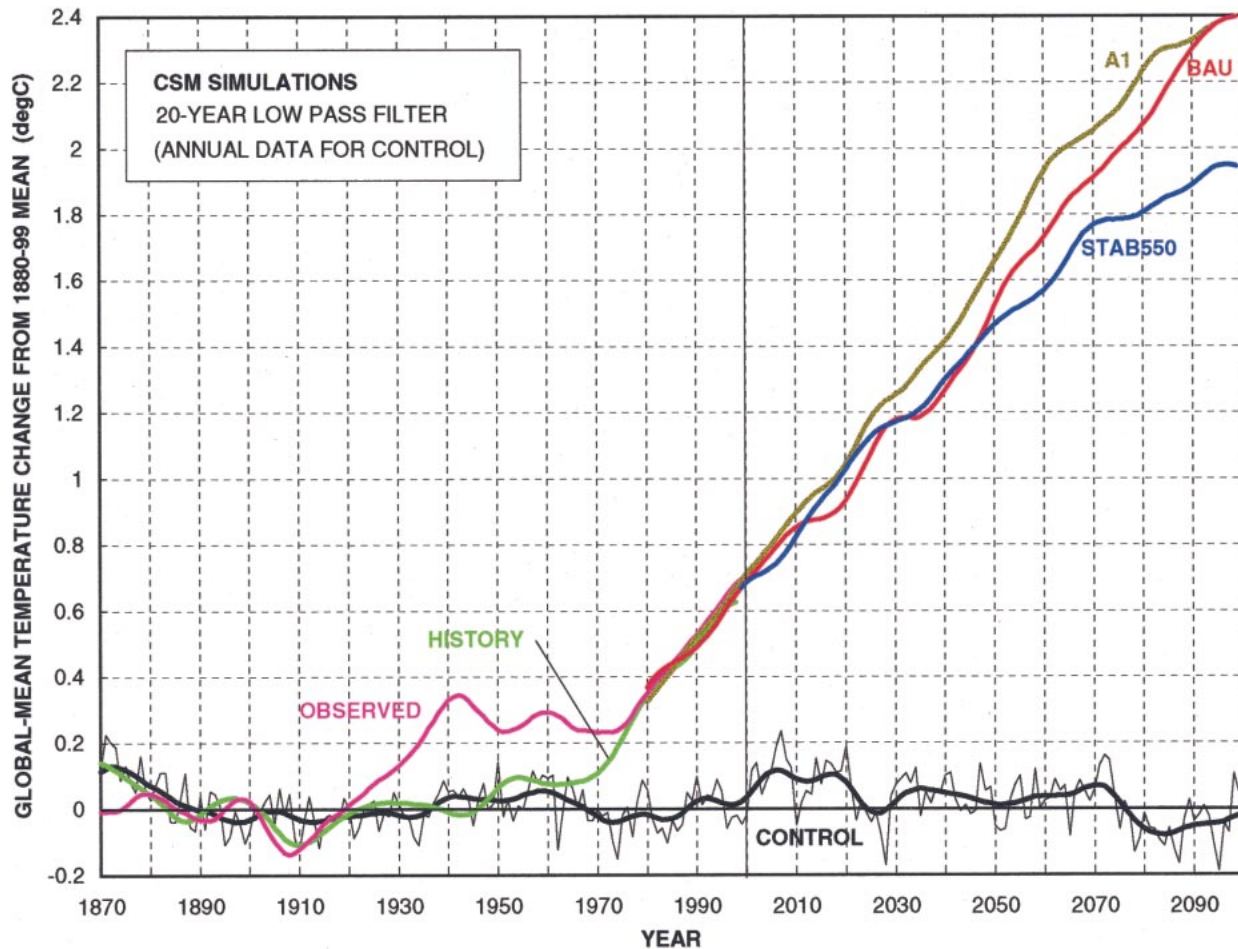


FIG. 17. Global mean air temperature changes ( $^{\circ}\text{C}$ ; thin curve, annual mean for the control run; thick curves, 20-yr low-pass filtered) at the reference height (2 m above all surfaces) from various CSM simulations. Black curves, control run; green curve, historical run; orange curve, BAU scenario; dark blue curve,  $\text{CO}_2$  stabilization at 550 ppmv (STA550) scenario; and yellow curve, IPCC SRES scenario A1. Also shown (pink curve) is observed global mean surface temperature anomaly from Nicholls et al. (1996 and updates).

similar to the BAU case except for a slightly higher (by  $\sim 0.1^{\circ}\text{--}0.2^{\circ}\text{C}$ ) temperature from the 2030s to the 2080s, when it has a higher  $\text{CO}_2$  and forcing level than the BAU scenario (cf. Fig. 1). In comparison, from 1890 to 1998 the global mean temperature increased by about  $0.7^{\circ}\text{C}$ , about half of the warming in the STA550 case.

By the early twenty-first century, the surface warming in both the BAU and STA550 runs is well above the range of internal variability of the model both globally (as exhibited by the control run—black curve in Fig. 17) and over all latitudinal zones except for  $60^{\circ}\text{--}90^{\circ}\text{S}$ , where the internal variability is large relative to the warming (Fig. 18). The warming signal to variability or noise ratio is largest over the low latitudes due to the small internal variations there. The warming trends averaged globally and over  $30^{\circ}$  zones are linear (Fig. 18). These linear trends are summarized by season in Table 1. In contrast, interdecadal variations in the observed global surface temperature during the twentieth century

(cf. Figs. 5 and 17) are considerably larger than those in the simulated twenty-first-century temperature (partly because the simulations did not include forcings other than greenhouse gases and sulfate aerosols), although the simulated variability is comparable between the two centuries.

Globally, the surface warming trend over 1980–2100 is about  $1.8^{\circ}\text{C century}^{-1}$  for the BAU scenario and  $1.4^{\circ}\text{C century}^{-1}$  for the  $\text{CO}_2$  stabilization scenario. The warming trend is about 40%–50% larger over land than over ocean (Table 1). From the 1990s to the 2090s, during which the atmospheric  $\text{CO}_2$  concentration approximately doubles in the BAU case (Fig. 1), the surface warming over the oceans is about  $1.0^{\circ}\text{--}2.0^{\circ}\text{C}$  except for the winter sea-ice regions, where the warming is substantially larger due to the strong positive feedback from melting of sea ice. The warming over the land surface is about  $1.5^{\circ}\text{--}3.0^{\circ}\text{C}$  (Fig. 19). The temperature changes from the 1990s to the 2090s (Fig. 19,

top) are significant at the 5% level over essentially all areas.<sup>3</sup>

The surface warming in the twenty-first century is largest (up to  $5.3^{\circ}\text{C century}^{-1}$ ) over the high latitudes (especially in winter) and smallest ( $\sim 1.0^{\circ}\text{C century}^{-1}$ ) over the Southern Hemisphere mid- and low latitudes (a minimum around  $60^{\circ}\text{S}$ ), where oceanic areas predominate (Table 1 and Figs. 18 and 19). The enhancement of warming at high latitudes, in particular over the northern North Atlantic, is largely due to the melting of excess sea ice (which induces a strong positive feedback) and the strong atmospheric stability there (which tends to confine the warming to the lower troposphere; Fig. 19). Smaller warming over the ocean surface is expected because evaporation and vertical mixing within the ocean both act to reduce the surface temperature rise in response to enhanced heating from greenhouse gases.

The latitudinal patterns of warming seen here, including the minimum around  $60^{\circ}\text{S}$ , are common in coupled climate model simulations (Kattenberg et al. 1996; Roeckner et al. 1999; Boer et al. 2000), but they differ from those for the equilibrium response to doubling of  $\text{CO}_2$ , which show increasing warming away from the equator (Mitchell et al. 1990). However, the warming over the northern North Atlantic in the CSM ( $\sim 3^{\circ}\text{--}5^{\circ}\text{C}$ ) is larger than that in the Hadley Centre and Canadian coupled GCMs (Mitchell et al. 1998; Boer et al. 2000). The ubiquitous warming in the CSM (as well as in the HadCM3 and Canadian models) is in contrast to Russell and Rind (1999) who find significant cooling over the North Atlantic and South Pacific in a transient coupled GCM run at the time of doubling of atmospheric  $\text{CO}_2$ , primarily due to a 30% slowdown in the thermohaline circulation.

In many coupled GCMs [e.g., Cubasch et al. 1992; Manabe and Stouffer 1994; Wood et al. 1999; Russell and Rind 1999; Boer et al. 2000; of which only HadCM3 (Wood et al. 1999) and the Goddard Institute for Space Studies (GISS) model (Russell and Rind 1999) did not use flux adjustments], the thermohaline circulation over the North Atlantic weakens in response to increased  $\text{CO}_2$  forcing mainly because of increased freshwater fluxes over this region. In a control run, the CSM produces large variability at timescales of 8–12 yr and 30–50 yr in the thermohaline structure and circulation in the North Atlantic (Capotondi and Holland 1998). The meridional overturning in the main North Atlantic cell de-

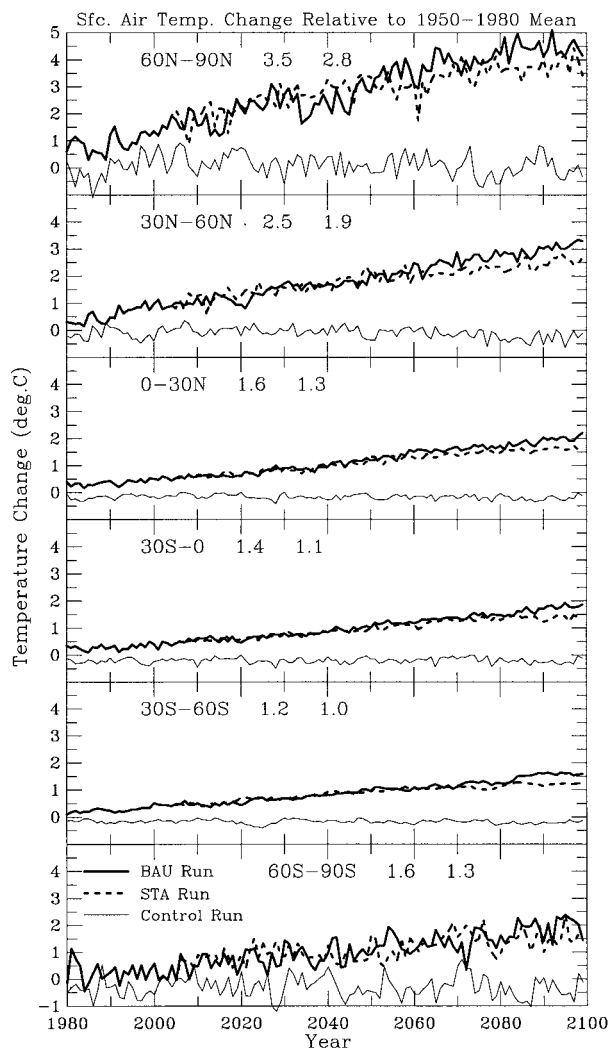


FIG. 18. Annual surface air temperature changes (relative to the 1950–80 mean) averaged over  $30^{\circ}$  latitudinal zones during the 1980–2099 period from the BAU (thick solid curve), STA550 (broken curve), and control (thin solid curve) runs. The numbers after the latitude label are the linear trends in  $^{\circ}\text{C century}^{-1}$  for the BAU and STA550 runs, respectively.

creases by only about 3% at the time of doubling of atmospheric  $\text{CO}_2$  content while the overturning in the Greenland–Iceland–Norwegian Sea region decreases by 50% (Meehl et al. 2000a). Results of Meehl et al. (2000a) and Russell and Rind (1999) suggest that the relatively large warming over the North Atlantic in the CSM (compared with the HadCM3, the Canadian model, and the GISS model) is partly due to the small changes in the main thermohaline circulation in the region (in addition to the strong sea-ice effect mentioned above).

The patterns of seasonal and vertical variations of the warming (Fig. 19) are similar to those seen in equilibrium GCM simulations (e.g., Hansen et al. 1984). Due to sea-ice feedback, and to the large seasonal cycle of atmospheric stability, the warming at high latitudes is

<sup>3</sup> The statistical significance of the linear trends is based on Student's *t*-tests (autocorrelations were accounted for according to Woodward and Gray 1993). The significance of changes in decadal or 20-yr means is derived using empirical sampling distributions of decadal or 20-yr means derived from the 230-yr control run. For example, if the temperature change from the 1990s to the 2090s at a particular grid box is  $2.0^{\circ}\text{C}$  and this change corresponds to the 95th or higher percentile in the histogram of decadal temperature changes in the control run, then this temperature change is considered as statistically significant at the 5% level.



TABLE 1. Seasonal and annual trends ( $^{\circ}\text{C century}^{-1}$ ) of surface air temperature from 1980 to 2099 averaged over  $30^{\circ}$  lat zones and over all land (land) and oceanic areas (ocean) and the globe (global) from the BAU and  $\text{CO}_2$  stabilization (in parentheses) simulations. All trends are statistically significant at the 5% level.

	60°–90°S	30°–60°S	0°–30°S	0°–30°N	30°–60°N	60°–90°N	Land	Ocean	Global
DJF	1.26 (1.11)	1.30 (1.00)	1.32 (1.08)	1.61 (1.26)	2.71 (2.03)	5.31 (3.84)	2.54 (1.84)	1.65 (1.32)	1.91 (1.47)
MAM	1.64 (1.35)	1.24 (0.96)	1.38 (1.10)	1.57 (1.26)	2.29 (1.73)	3.39 (2.89)	2.15 (1.65)	1.55 (1.25)	1.72 (1.37)
JJA	1.83 (1.47)	1.23 (0.96)	1.48 (1.18)	1.55 (1.25)	2.43 (1.97)	1.49 (1.24)	2.08 (1.71)	1.46 (1.16)	1.64 (1.32)
SON	1.55 (1.10)	1.20 (0.93)	1.45 (1.15)	1.62 (1.30)	2.35 (1.91)	4.00 (3.16)	2.33 (1.84)	1.57 (1.25)	1.79 (1.42)
ANN	1.57 (1.25)	1.24 (0.96)	1.41 (1.12)	1.59 (1.27)	2.45 (1.91)	3.54 (2.78)	2.28 (1.76)	1.56 (1.24)	1.77 (1.39)

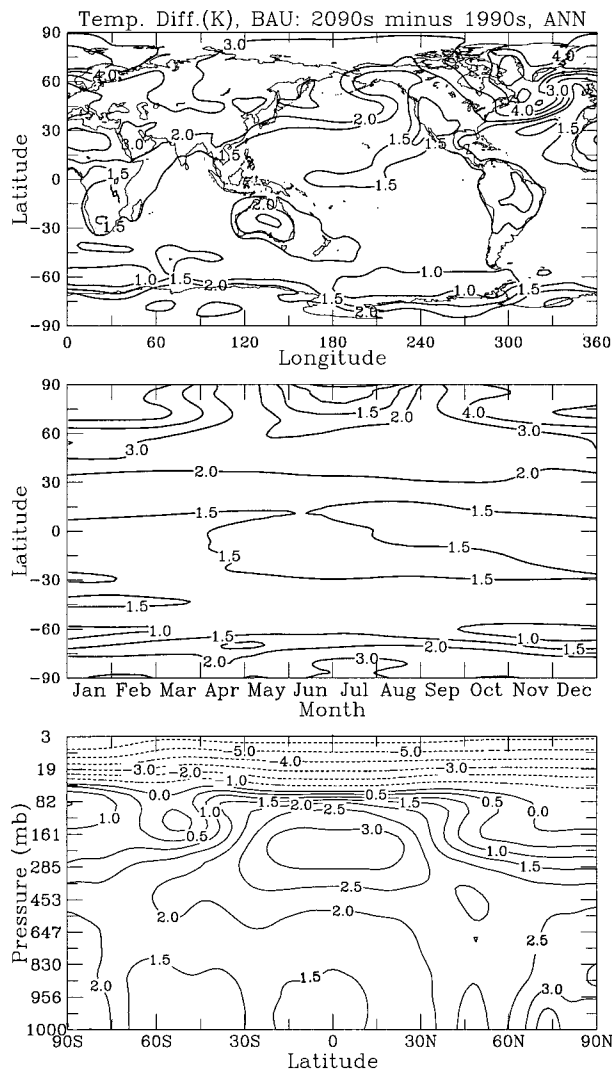


FIG. 19. Air temperature change from the 1990s to the 2090s in the BAU run: (top) the geographical distribution of annual mean surface air warming, (middle) the seasonal variation of the surface air warming averaged over longitude, and (bottom) shows the vertical distribution of the temperature change averaged over season and longitude.

much larger in winter than in summer. At low latitudes, the warming is largest in the upper troposphere ( $\sim 3.0^{\circ}\text{C}$ ). Over much of the troposphere, atmospheric temperature increases (due to enhanced longwave heating by  $\text{CO}_2$  and other greenhouse gases) by about  $1.5^{\circ}$ – $2.0^{\circ}\text{C}$  from the 1990s to the 2090s in the BAU case (Fig. 19). Note that the tropospheric warming extends up into the lower stratosphere, especially in the Southern Hemisphere south of  $\sim 30^{\circ}\text{S}$ , probably as a result of the model-simulated recovery of the ozone layer. Seasonal plots (not shown) revealed that the warming in the mid- and upper troposphere has little seasonal variation, except over the polar regions where the warming extends well above the tropopause in winter. A cooling (due to enhanced radiative cooling of increased  $\text{CO}_2$ ) up to  $6.0^{\circ}\text{C}$  occurs in the midstratosphere.

It has been suggested that the enhanced warming in the upper troposphere in the Tropics, a common feature in many GCMs, results from enhanced latent heating from more vigorous moist convection under a warmer climate (e.g., Hansen et al. 1984; Mitchell 1989). Our results, however, indicate that latent heating may not be the only cause. As shown later (cf. Fig. 26 later), zonal mean precipitation (a proxy for latent heating) decreases around the zone  $10^{\circ}$ – $15^{\circ}$  from the equator in the summer hemisphere, accompanied by a general decrease in the intensity of the zonal mean Hadley circulation (cf. Fig. 36 later; consistent with the increased static stability resulting from temperature profile changes in the Tropics). Precipitation does not increase over the subtropics (cf. Fig. 26 later), and a noticeable increase in zonal mean precipitation occurs only around  $5^{\circ}$  from the equator in the summer hemisphere. This implies that the zone of enhanced latent heating in the Tropics is both spatially and seasonally limited, and does not extend into the subtropics. On the other hand, the enhanced upper-tropospheric warming extends to midlatitudes in summer (not shown) and the annual mean. While advection can contribute to the smoothness of the warming pattern in the upper troposphere, it is unlikely that the latent heating changes at low latitudes alone can generate this widespread warming pattern. We suggest that (infrared) radiative effects of cloudiness and water vapor changes

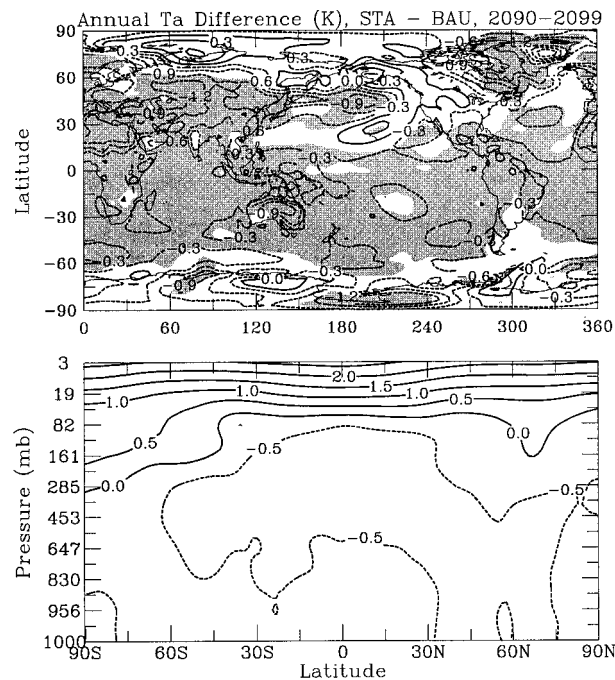


FIG. 20. (top) Geographical and (bottom) vertical distribution of the STA550 minus BAU difference of annual mean air temperature during 2090–99. The shading in (top), which is for the temperature difference at the surface, indicates that the difference is statistically significant at a 5% level.

(Figs. 31 and 30 later) play an important role in generating the enhanced warming in the upper troposphere at low and midlatitudes. We will return to this issue in section 5c.

The reduction in warming that results from stabilizing the  $\text{CO}_2$  concentration at 550 ppmv is seen over most of the globe (Fig. 20), although the reduction is larger over land than over ocean, and statistically significant only over the mid- and low latitudes. The  $\text{CO}_2$  stabilization reduces the tropospheric warming over the twenty-first century by about  $0.5^\circ\text{C}$  and the midstratospheric cooling by about  $1.0^\circ\text{--}2.0^\circ\text{C}$  (Fig. 20). However, the warming in the upper troposphere at  $60^\circ\text{--}90^\circ\text{S}$  is actually  $\sim 0.5^\circ\text{C}$  larger in the STA550 case than in the BAU case.

Under the BAU scenario, the enhanced warming at high latitudes reduces the DJF meridional temperature gradient at the surface by about  $0.1^\circ\text{--}0.2^\circ\text{C}$  per degree of latitude ( $\sim 15\%\text{--}20\%$ ) from the 1990s to the 2090s over  $50^\circ\text{--}70^\circ\text{N}$  (slightly smaller changes occur in the STA550 case; Fig. 21). The changes in the temperature gradient are relatively small in other seasons and over other latitudes. They are also small in the free troposphere (cf. Fig. 19).

Because of the differential temperature change with height, the temperature profile or lapse rate in the 2090s can differ substantially from that of the 1990s. Figure 22 shows these profile changes over land and ocean areas for different zones. In general, the warming at the surface and the lower troposphere is larger over land

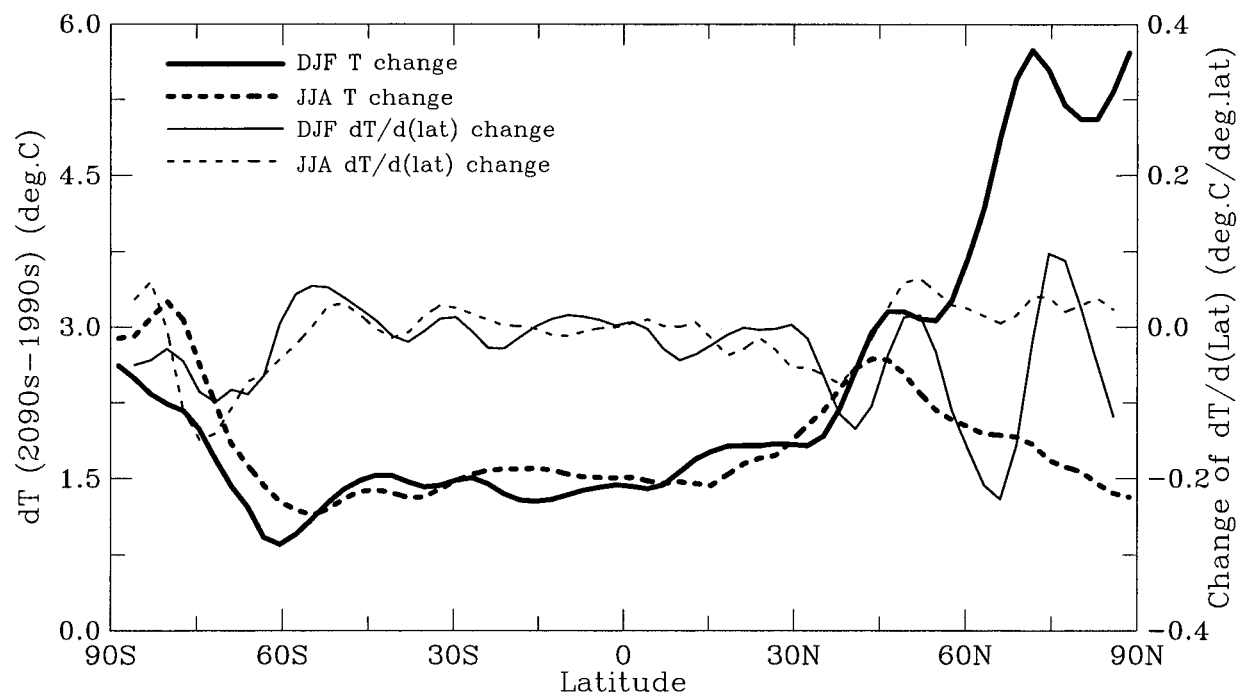


FIG. 21. Latitudinal distribution of changes of DJF (thick solid curve), and JJA (thick broken curve) zonal mean surface air temperature from 1990–99 to 2090–99 in the BAU run. Also shown (read on the right side ordinate) are the changes (2090s minus 1990s) of Pole-to-equator gradient of surface air temperature ( $^\circ\text{C}$  per degree of lat) for DJF (thin solid curve) and JJA (thin broken curve).

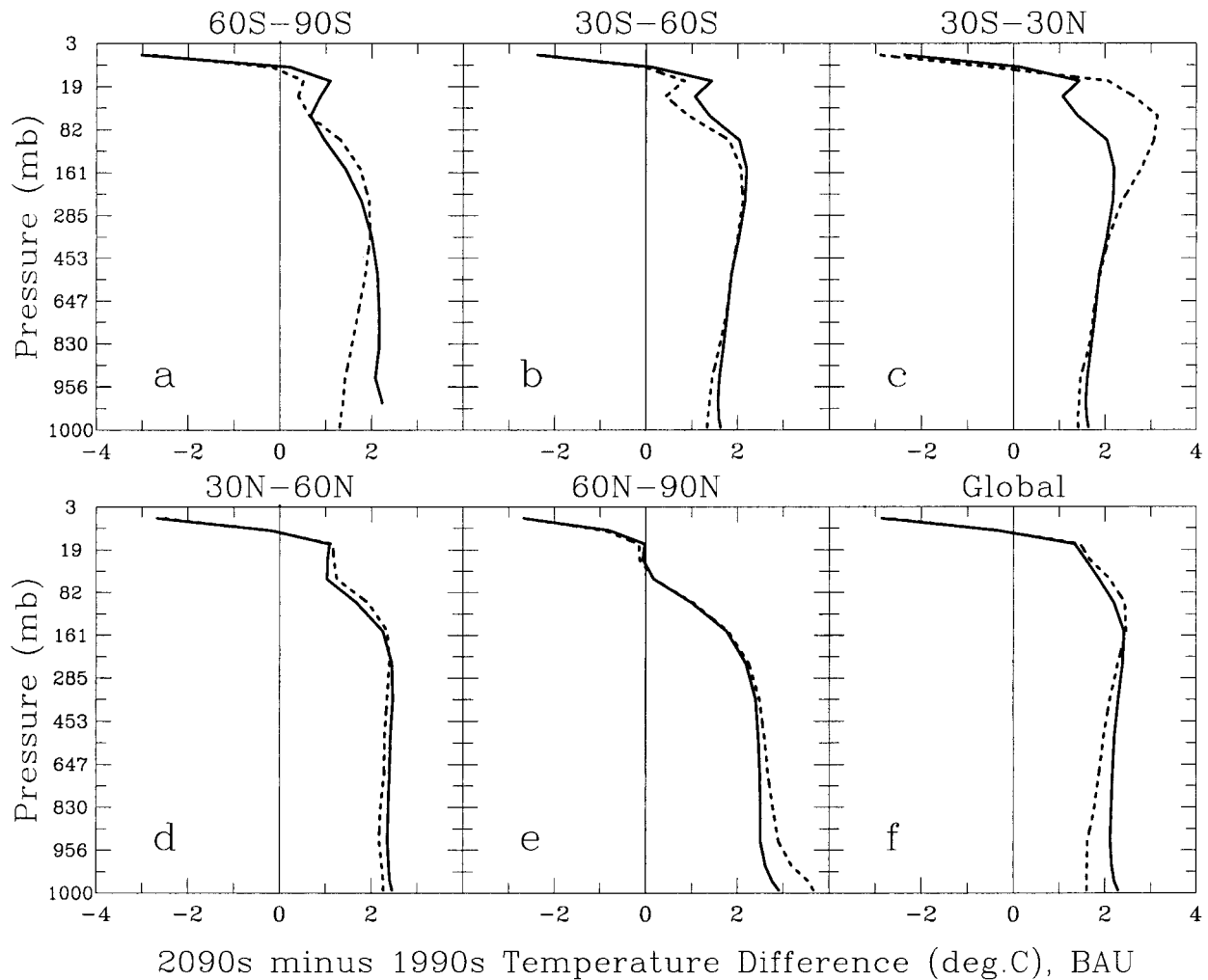


FIG. 22. Vertical profiles of annual temperature changes from the 1990s to the 2090s in the BAU simulation averaged over land (solid curve) and oceanic (dashed curve) areas: (a) 60°–90°S; (b) 30°–60°S; (c) 30°S–30°N; (d) 30°–60°N; (e) 60°–90°N; and (f) over the globe.

than over ocean, except for the northern high latitudes where the warming over the ocean is greater than over the land areas because of melting sea ice. Over the land areas, there is little change in lapse rate in the mid- and lower troposphere. Over most of the oceanic areas, however (except for 60°–90°N and 30°–60°N, where there is relatively little ocean), there is a decrease in lapse rate, reflecting increased evaporation at the surface (cf. Fig. 29) and enhanced latent heating at higher levels. The change in lapse rate is accompanied by a change in vertical distribution of specific humidity (larger percentage increases in the upper troposphere, cf. Fig. 30 later). The effects of changes in lapse rate and in the vertical distribution of water vapor tend to cancel each other (Hansen et al. 1984).

The simulated warming over the next century will have considerable implications for our daily life. To judge these consequences, we need to examine the details of change at subcontinental scales. For example,

over most of the contiguous United States, the number of summer (JJA) hot days, defined as the days with daily maximum temperature ( $T_{\max}$ ) equal to or exceeding the 80th percentile of current (1980–99) summer daily  $T_{\max}$ , will double by the 2090s (from ~20 today to ~40 in the 2090s; Fig. 23). Ignoring autocorrelation effects, this means that the probability of three consecutive hot days (defined by this threshold) will increase from ~1% to ~8% over the next 100 yr. Such an increase in the frequency of extreme temperatures, when combined with increased specific humidity (Fig. 30 later), would lead to much more frequent occurrence of severe heat stress conditions in U.S. cities during summer (see, e.g., Gaffen and Ross 1998; Delworth et al. 1999).

#### *b. Precipitation, evaporation, and soil moisture changes*

Figure 24 shows the global mean precipitation rate simulated in the control, BAU, CO<sub>2</sub> stabilization, and

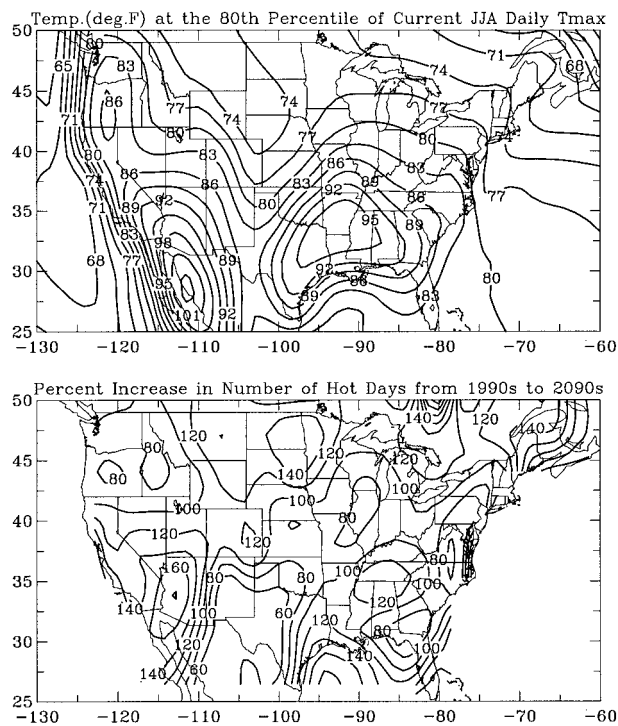


FIG. 23. (top) Daily maximum temperature ( $^{\circ}\text{F}$ ) at the 80th percentile of summer (JJA) daily maximum temperature for 1980–99 over the contiguous United States. (bottom) Percentage increase of the number of summer hot days (with daily maximum temperature equal to or exceeding that shown in the top) from the 1990s to the 2090s under the BAU scenario (similar increases occur under the  $\text{CO}_2$  stabilization scenario).

IPCC SRES scenario A1 runs. In the control run, the simulated precipitation is around  $2.980 \pm 0.015 \text{ mm day}^{-1}$ , remaining fairly stable during the 230-yr integration period. Accompanying the rapid rise in global mean temperature after the late 1970s (Fig. 17), global mean precipitation increases steadily in all the other runs at a small ( $\sim 0.142 \text{ mm day}^{-1} \text{ century}^{-1}$ ) but statistically significant rate. This is in agreement with other transient coupled GCM experiments (Kattenberg et al. 1996). By the late 1990s, the global mean precipitation is well above the range of internal variability of the model. (Such a change, however, may not be detectable in the observational record because of the lack of any long-term, global mean precipitation data.) The global mean precipitation rate is indistinguishable in the BAU, STA550, and IPCC SRES A1 scenarios until the 2060s when the STA550 scenario diverges to a slightly lower rate of increase. The global mean precipitation rates generally follow the increases of global mean temperature, with noticeable decadal variations (Fig. 24).

The increase in global mean precipitation comes primarily from increases in winter precipitation over northern mid- and high latitudes, a common feature in other coupled GCMs (Kattenberg et al. 1996), with some contribution from the southern high latitudes (Figs. 25 and 27). Precipitation changes are highly variable at low

latitudes, and the increases in these latitudes are generally small relative to the model's internal variability (Fig. 25). This is in sharp contrast to the zonal temperature changes (Fig. 18), which have the largest signal-to-noise ratio at low latitudes. Compared with 1980–99, 2080–99 shows large increases (30%–50%) over India and Pakistan, the Arabian Peninsula, the southwestern U.S.A., and Greenland. (The latter is an important factor for the mass balance of the ice sheet, but CSM results here are less reliable because of the sea ice problem noted earlier.) The largest percentage decreases (20%–50%) in precipitation are found in northeastern Africa and the eastern Mediterranean (Fig. 27).

The latitudinal pattern of precipitation changes is shown in Fig. 26. It can be seen that zonal mean precipitation increases poleward of  $\sim 40^{\circ}$ . Over the subtropics ( $20^{\circ}$ – $40^{\circ}$ ), summer precipitation increases while winter precipitation decreases, resulting in little change in annual precipitation. In the Tropics ( $20^{\circ}\text{S}$ – $20^{\circ}\text{N}$ ), the changes are more complicated. As noted earlier, over the summer hemisphere (i.e., the Northern Hemisphere in JJA and the Southern Hemisphere in DJF), precipitation shows a zone of increase around  $5^{\circ}$  from the equator and decreases around  $10^{\circ}$ – $15^{\circ}$  from the equator. These tropical precipitation changes are related to the changes in the Hadley circulation discussed below.

The precipitation increases over  $60^{\circ}$ – $90^{\circ}\text{N}$  and  $60^{\circ}$ – $90^{\circ}\text{S}$  zones, which occur in both winter and summer, are associated with the large warming at these latitudes at the surface and in the lower troposphere (Fig. 19). The warming increases lower-tropospheric water vapor content substantially; for example, by 30%–60% over the northern high latitudes in winter (Fig. 30 later). Since atmospheric water vapor content is closely linked to stratiform precipitation in the CSM (Kiehl et al. 1996), the water vapor increases result in similar percentage increases in large-scale precipitation (not shown). These increases account for most of the total precipitation increases at high latitudes. In comparison, available observations show increased precipitation during the twentieth century over northern mid- and high-latitude land areas (Dai et al. 1997a).

Under the STA550 scenario, precipitation averaged over 2080–99 is about 10% less than that in the BAU run over much of Eurasia, but the differences are noisy and generally small (within  $\pm 10\%$ ) on regional scales ( $10^2$ – $10^3 \text{ km}$ , not shown). Although the changes in zonal mean precipitation are fairly stable, as shown by the similar trends in the BAU and STA550 runs (Fig. 25), on regional scales precipitation changes by the end of the twenty-first century are still very noisy, especially for seasonal averages and over the low latitudes (Fig. 27 illustrates this for the BAU case). For example, over the southwestern United States during winter, 2080–99 is wetter than 1980–99 in the BAU case (Fig. 27), whereas it is the opposite in the STA550 case (not shown). This difference is, however, not statistically significant due to the large decadal variability over this



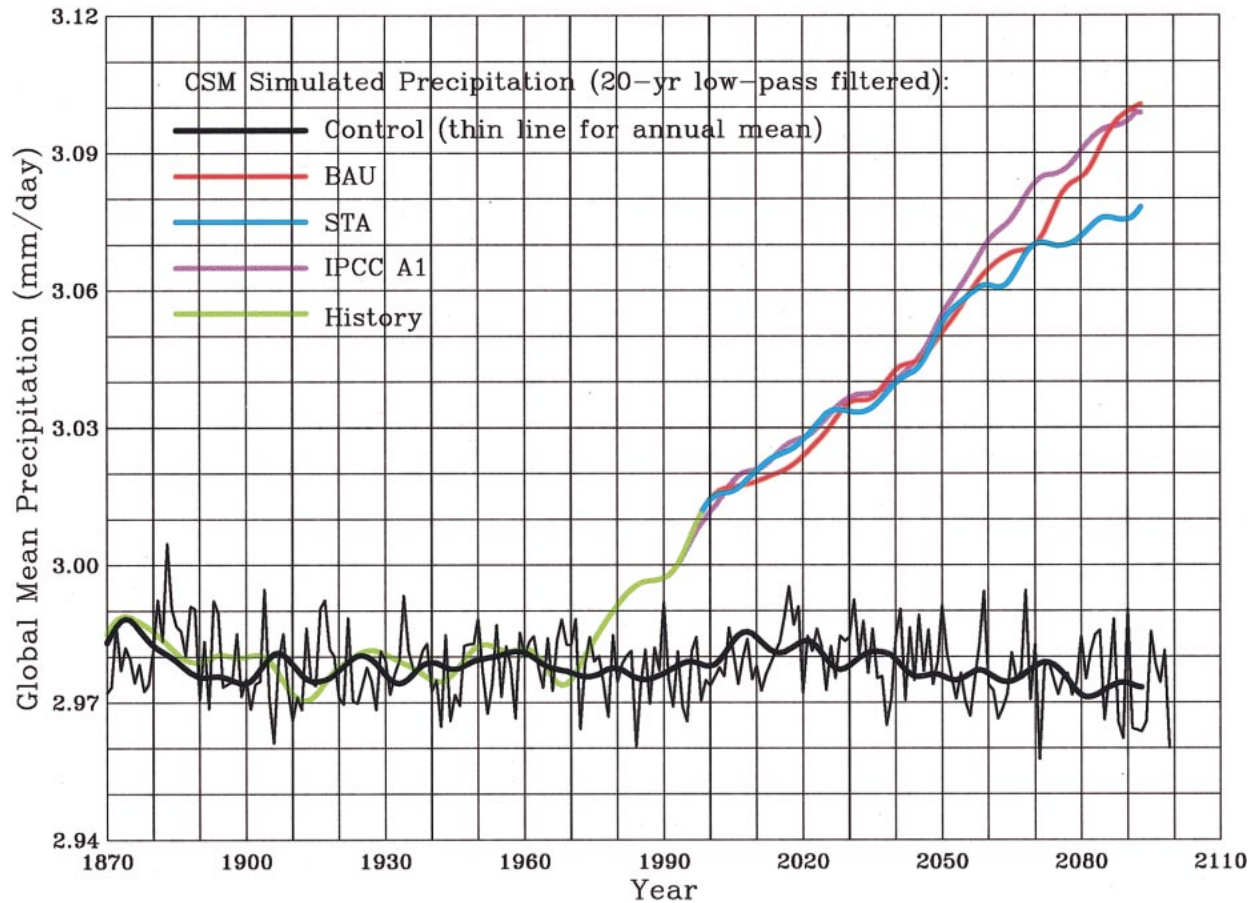


FIG. 24. Global mean precipitation rate ( $\text{mm day}^{-1}$ ) from various CSM simulations from 1870 to 2099.

region. Indeed, over the twenty-first century as a whole, the trends in winter precipitation over the southwestern United States, as well as over the whole contiguous United States (Fig. 28), are not statistically significant. The increasing trends of summer and annual precipitation averaged over the contiguous United States are, however, statistically significant at the 5% level (Fig. 28).

Surface evaporation (and latent heat flux) increases steadily in tandem with surface temperature at all latitudes except for  $60^{\circ}$ – $90^{\circ}$ S, where the changes are small (Fig. 29). Evaporation increases over most land and oceanic areas, especially over regions with melting sea ice (e.g., the western North Atlantic). Since precipitation increases at low latitudes are relatively small (Fig. 25), the increased water vapor resulting from enhanced evaporation over low latitudes is transported into mid- and high latitudes and returned to the surface through increased precipitation at these latitudes, as noted in previous studies (e.g., Manabe and Stouffer 1994). Figures 25 and 29 therefore imply that the atmospheric poleward and oceanic equatorward transport of water is increased from the 1990s to the 2090s (due to the general increase in atmospheric specific humidity). The increase is

around 30%–40% based on a mean meridional transport of  $6$ – $9 \text{ mm month}^{-1}$  over 1950–80 (the difference between evaporation and precipitation averaged over  $30^{\circ}\text{S}$ – $30^{\circ}\text{N}$ ) and a change of  $2.6$ – $3.1 \text{ mm month}^{-1}$  from the 1990s to the 2090s.

Changes in soil moisture content (not shown) are generally small (within  $\pm 3\%$  for annual mean) by the 2090s over most land areas. There is a slightly increase ( $\leq 3\%$ ) in soil moisture content at northern mid- and high latitudes during winter and in the annual mean in response to increased precipitation there (partly offset by enhanced evaporation). This is in agreement with other transient GCM experiments (Kattenberg et al. 1996). During summer, soil moisture content decreases (by 3%–6%) over eastern Europe, western Asia, and much of Canada, but increases over central Russia and the central United States. At low latitudes ( $30^{\circ}\text{S}$ – $30^{\circ}\text{N}$ ), the sign of changes in soil moisture content tends to follow that of precipitation changes and the magnitude of the changes can be 10%–20% from the 1990s to the 2090s over areas with large precipitation changes, such as central Australia, northwestern India, and the Sahel (cf. Fig. 27).

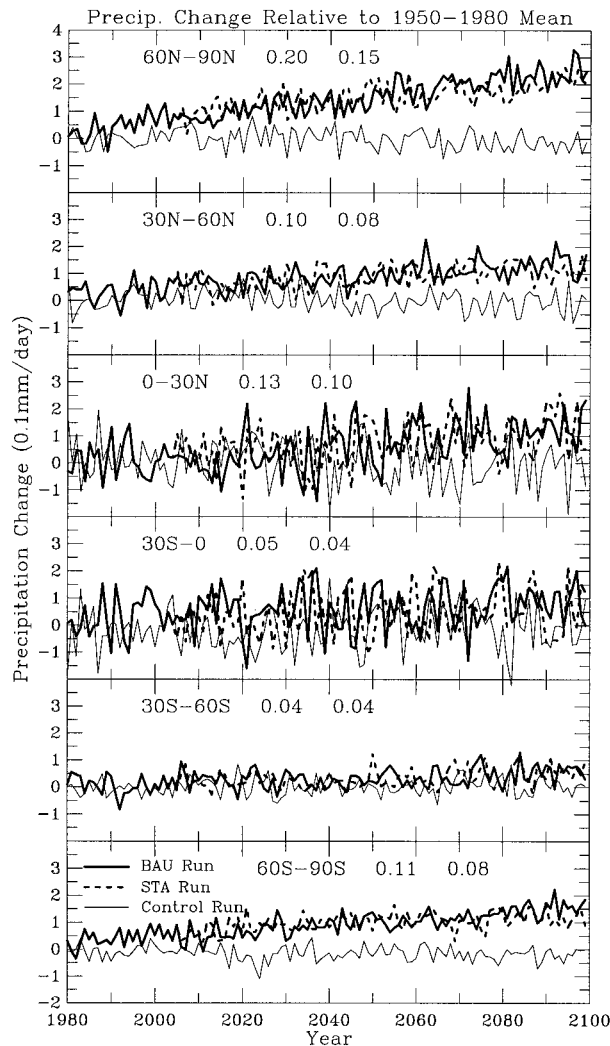


FIG. 25. Same as Fig. 18, but for annual precipitation. The unit for trends is  $\text{mm day}^{-1} \text{ century}^{-1}$ .

*c. Water vapor, cloudiness, and diurnal temperature range changes*

Atmospheric water vapor content (specific humidity) increases in the troposphere as air temperature rises (Fig. 30), reflecting relatively small changes in relative humidity. In accordance with the nonlinear temperature dependence of the Clausius–Clapeyron equation, most of the increased water vapor amount is concentrated in the lower troposphere (below 700 mb) over the low latitudes, where specific humidity increases by  $1.0\text{--}1.5 \text{ g kg}^{-1}$  from the 1990s to the 2090s. However, the percentage increases of water vapor are much larger in the upper troposphere and over (winter) high latitudes ( $\sim 30\%\text{--}60\%$ ) than in the lower troposphere over the low latitudes ( $\sim 10\%$ ; Fig. 30). Patterns of change are similar to those for temperature changes (cf. Fig. 19) and are similar to those in other GCM simulations (Mitchell et al. 1990; Kattenberg et al. 1996).

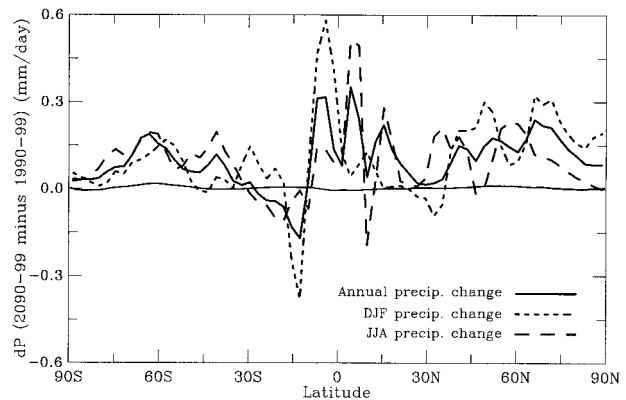


FIG. 26. Latitudinal distribution of zonally averaged precipitation changes ( $\text{mm day}^{-1}$ ) from the 1990s to the 2090s simulated by the CSM under the BAU scenario (similar under the STA550 scenario).

Total cloud cover (derived using random overlap) changes little over most areas from the 1990s to the 2090s in both the BAU and STA550 runs (not shown). However, there is a redistribution of cloudiness in the atmosphere, namely an increase (of  $0.5\%\text{--}1.0\%$  of absolute sky cover) in high clouds and a comparable decrease in middle clouds (Fig. 31). This upward shift in cloudiness, which is more pronounced in summer than in winter, is evident at all latitudes. It results primarily from more vigorous moist convection in a warmer climate in which there is more water vapor (cf. Fig. 30) and, consequently, more latent heat release to drive air parcels to higher levels (and form clouds there). There are also some decreases in low-level clouds over high latitudes (primarily in winter), due to the reduction in relative humidity that occur in these regions. Over low and midlatitudes, there is a slight increase ( $\sim 0.5\%$ ) in low-level clouds. The cloud change patterns are similar in both the BAU and STA550 runs, and similar to those in other GCM simulations (Mitchell 1989; Kattenberg et al. 1996).

Increased cloudiness and water vapor (Fig. 30) in the upper troposphere can significantly enhance longwave radiative heating in the upper troposphere. For example, moving all clouds into a single layer around 200 mb results in large warming below this layer in a GCM (Wang and Rossow 1998). The radiative effect of the cloudiness and water vapor changes is likely to be one of the main causes for the enhanced warming in the upper troposphere.

The changes in cloudiness and soil moisture have an effect on the diurnal temperature range (DTR) at the surface. It is well known that, since the 1950s, the DTR decreased over most of the continents (Nicholls et al. 1996; Easterling et al. 1997), a decrease that has been attributed primarily to increases in cloudiness (mostly clouds with low bases; Dai et al. 1997b, 1999). Coupled models in general produce decreased DTR over much of the midlatitude continents in response to increased  $\text{CO}_2$  and aerosols (Kattenberg et al. 1996). Under the



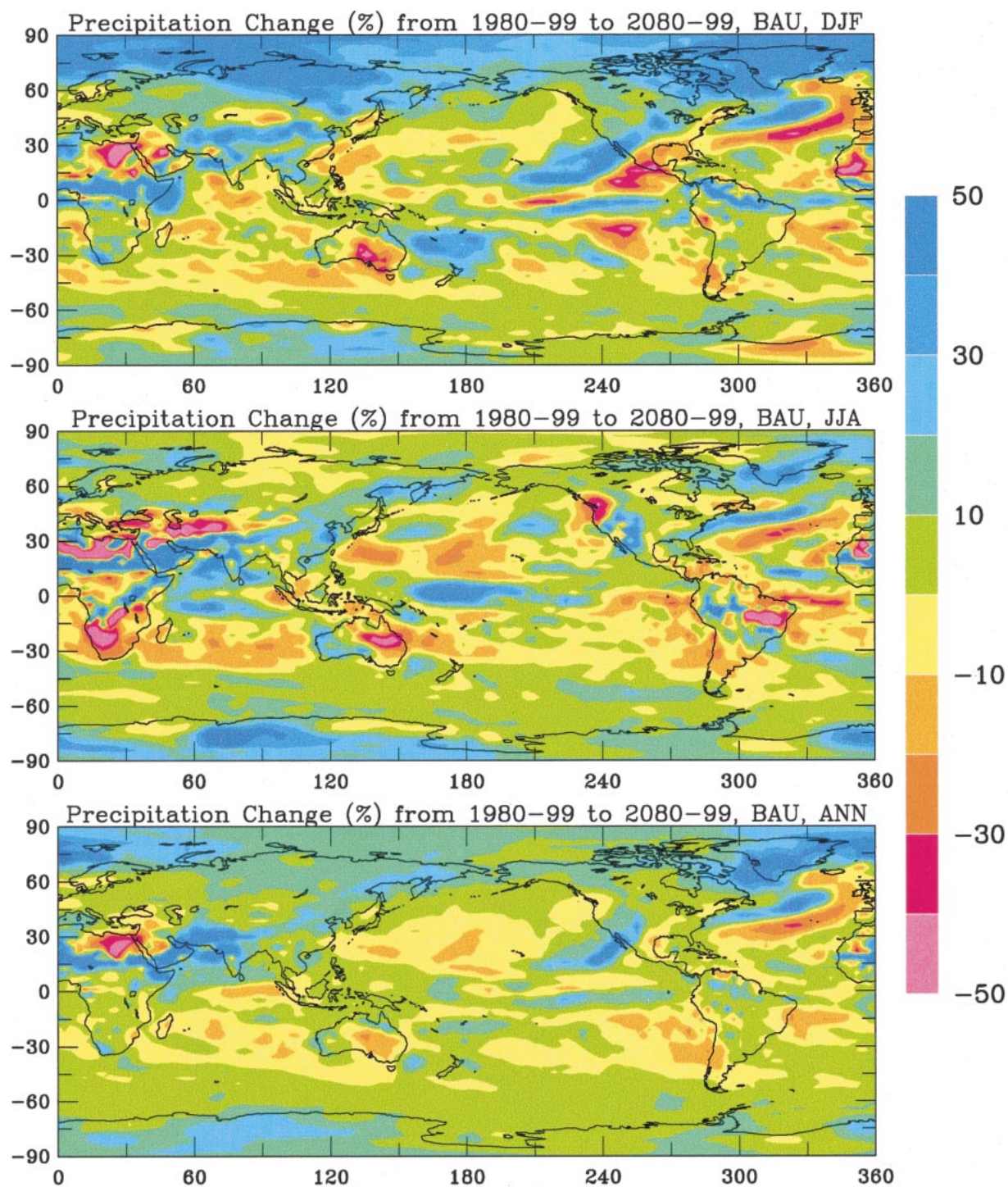


FIG. 27. Precipitation percentage change from 1980–99 to 2080–99 in the BAU simulation for (top) DJF, (middle) JJA, and (bottom) annual mean.

BAU scenario, the CSM-simulated DTR decreases by about  $0.2^{\circ}$ – $0.5^{\circ}\text{C}$  from the 1990s to the 2090s over most land areas. The exceptions (where the DTR increases by  $0.2^{\circ}$ – $1.0^{\circ}\text{C}$ ) are Australia, South Africa (JJA only),

and northern Africa (DJF only; Fig. 32). Similar changes occur under the STA550 scenario. The modeled DTR decreases over the midlatitude continents are associated with increases in precipitation, low-level cloudiness,



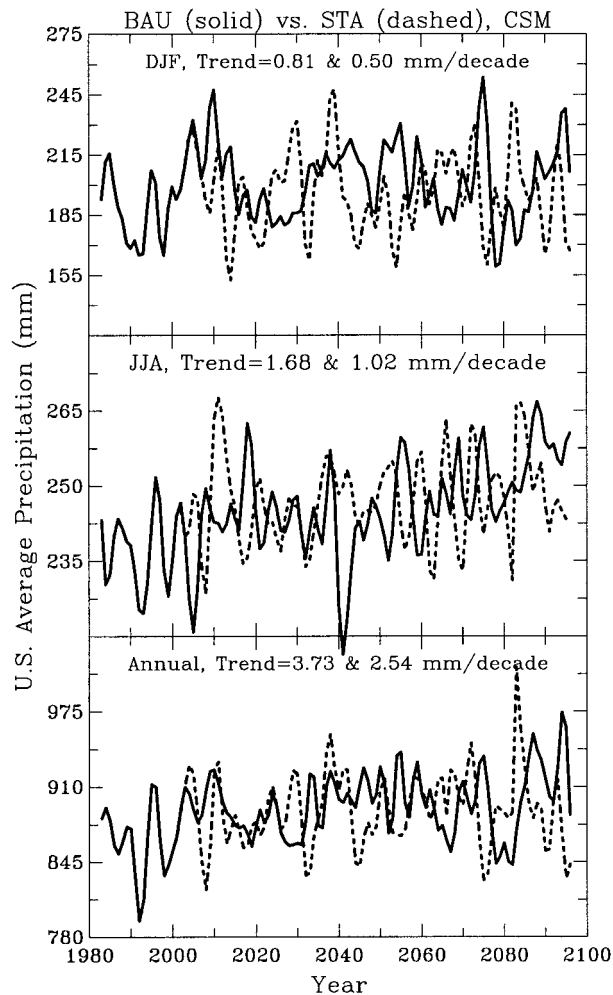


FIG. 28. (top) CSM-simulated DJF, (middle) JJA, and (bottom) annual mean precipitation averaged over the contiguous United States from 1980 to 2099. The solid curve is for the BAU scenario and the dashed curve for the STA550 scenario. Variations on shorter than 4-yr timescales were filtered out.

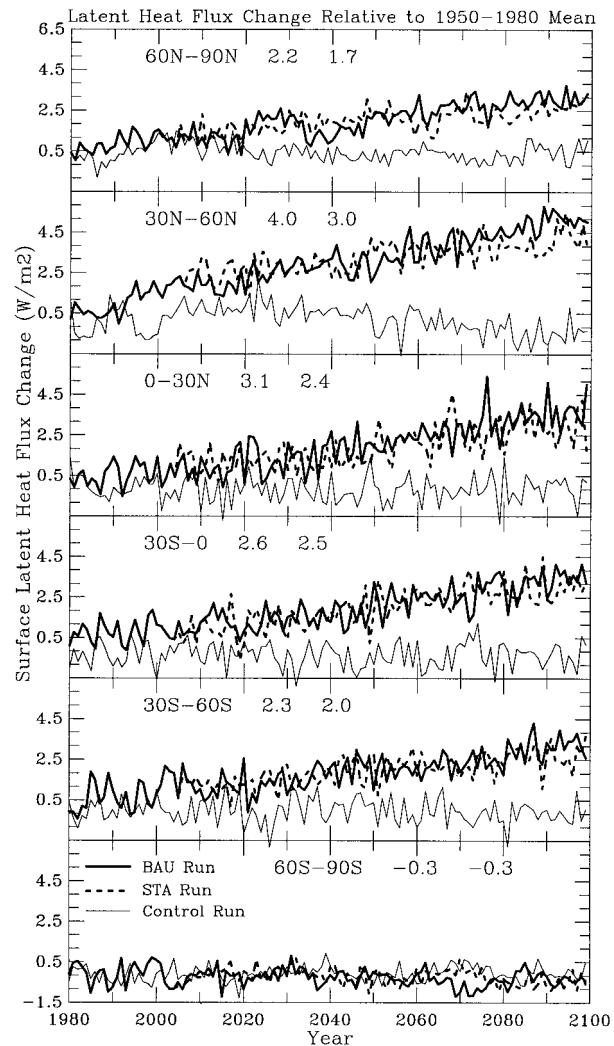


FIG. 29. Same as Fig. 18, but for annual surface latent heat flux. Surface evaporation in  $\text{mm month}^{-1}$  has approximately the same values as latent heat flux in  $\text{W m}^{-2}$ .

and soil moisture (although small), all of which have damping effects on the DTR in the current climate (Dai et al. 1999).

#### d. Atmospheric circulation changes

The enhanced warming at high latitudes (Figs. 18 and 21) and the changes in the vertical temperature profile (Figs. 19 and 22) could potentially induce important changes in atmospheric circulation. Here we present changes in synoptic storms (2–8-day timescale) and the zonal mean circulation from the 1990s to the 2090s under the BAU scenario. We also examined other decades and found similar change patterns. Changes under the STA550 scenario are similar to the BAU case.

Figure 33 shows percentage changes in the activity of synoptic storms under the BAU scenario (cf. Fig. 11 for the 1980s base state). In general, storm activity de-

creases (by up to 10%) at low latitudes and over mid-latitude oceans, including the areas of strongest DJF storm activity in the North Pacific and the North Atlantic. Over much of Eurasia and northern Canada, storm activity increases. Although most of the mid- to high-latitude precipitation increases, as noted earlier, are associated with large-scale precipitation changes in the model, there is still some correlation between the changes in DJF storm activity and precipitation (cf. Fig. 27) over northern mid- and high latitudes. For example, over the eastern North Pacific and southern Alaska, both DJF precipitation and storm activity decreases from 1990s to 2090s; whereas they both increase over the western United States, Russia, and northern Canada.

Figure 34 shows the 2090s minus 1990s difference in the zonally averaged zonal wind component under the BAU scenario. It can be seen that the largest changes

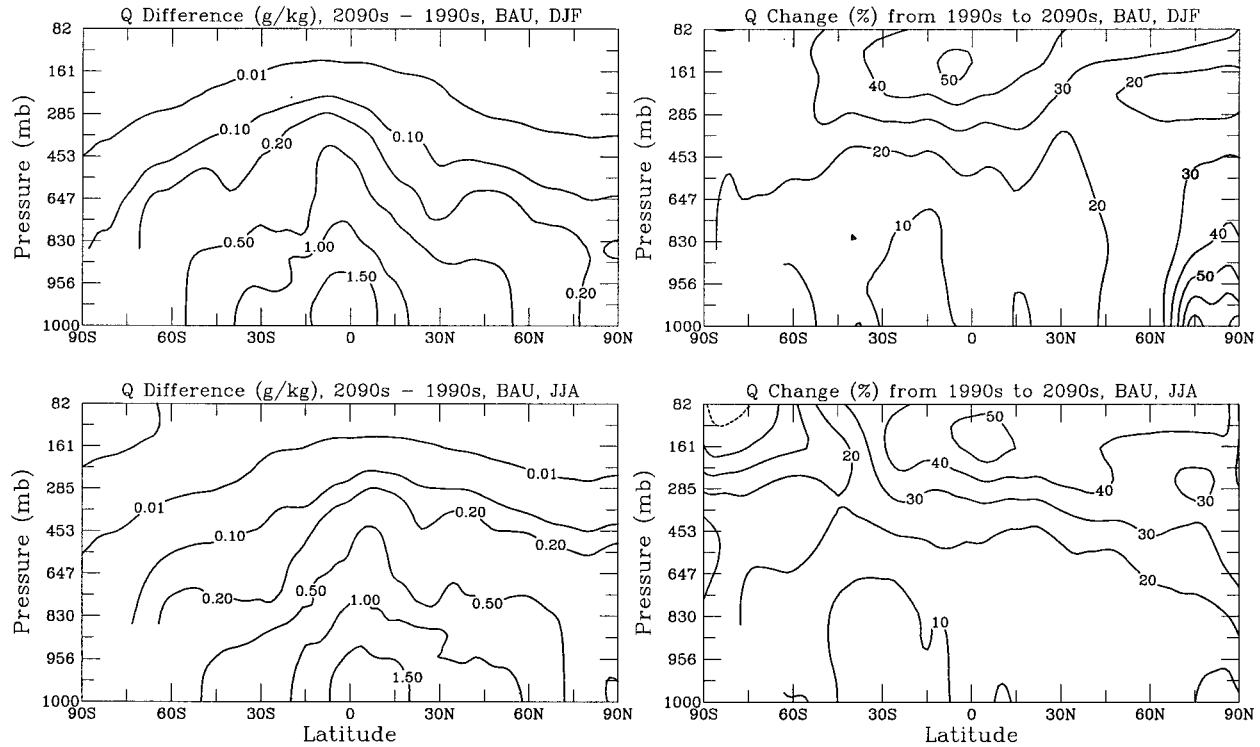


FIG. 30. Latitude–height distribution of specific humidity change from the 1990s to the 2090s in the BAU run averaged over longitude for (top) DJF and (bottom) JJA. (left) Absolute changes in  $\text{g kg}^{-1}$  and (right) changes expressed as a percentage of the 1990s mean.

are in the lower stratosphere (above  $\sim 80$  mb) and upper troposphere. The cores of the subtropical jets (cf. Fig. 12) appear to move slightly up- and equatorward, especially over the winter hemisphere. The westerlies in the lower stratosphere over the winter hemisphere also strengthen considerably (by  $\sim 10\%$ – $15\%$ ). Changes in the lower troposphere are small ( $\leq 0.5 \text{ m s}^{-1}$ ).

The mean meridional streamfunction (Fig. 35) and vertical pressure velocity (Fig. 36) suggest a decrease of  $\sim 10\%$  in the intensity of the Hadley circulation from the 1990s to the 2090s in the BAU simulation in both summer and winter (also seen in spring and autumn, not shown here). In spite of this decrease, however, Fig. 36 shows that the main equatorial convection zone ( $\sim 5^\circ$ – $8^\circ$

from the equator over the summer hemisphere) is stronger and penetrates higher in the 2090s than in the 1990s. This results in enhanced meridional mass transport around the tropopause (Fig. 35) and increased precipitation around these latitudes (cf. Fig. 26). The wintertime

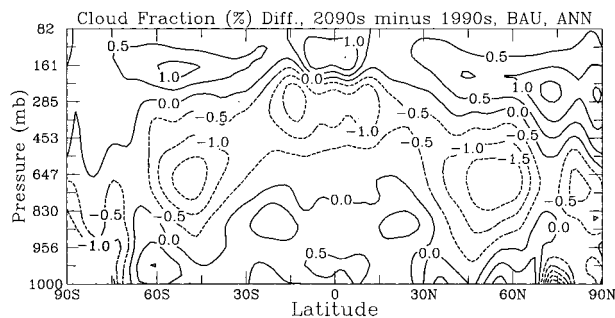


FIG. 31. Latitude–height distribution of changes of annual mean cloud amount (in % of the sky cover) from the 1990s to the 2090s in the BAU run.

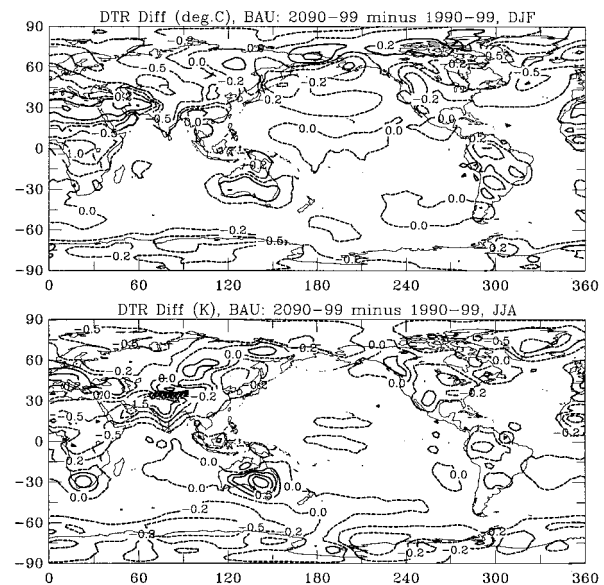


FIG. 32. Change in the diurnal range of surface air temperature ( $^\circ\text{C}$ ) from the 1990s to the 2090s for (top) DJF and (bottom) JJA in the BAU run (similar changes occur in the STA550 run).

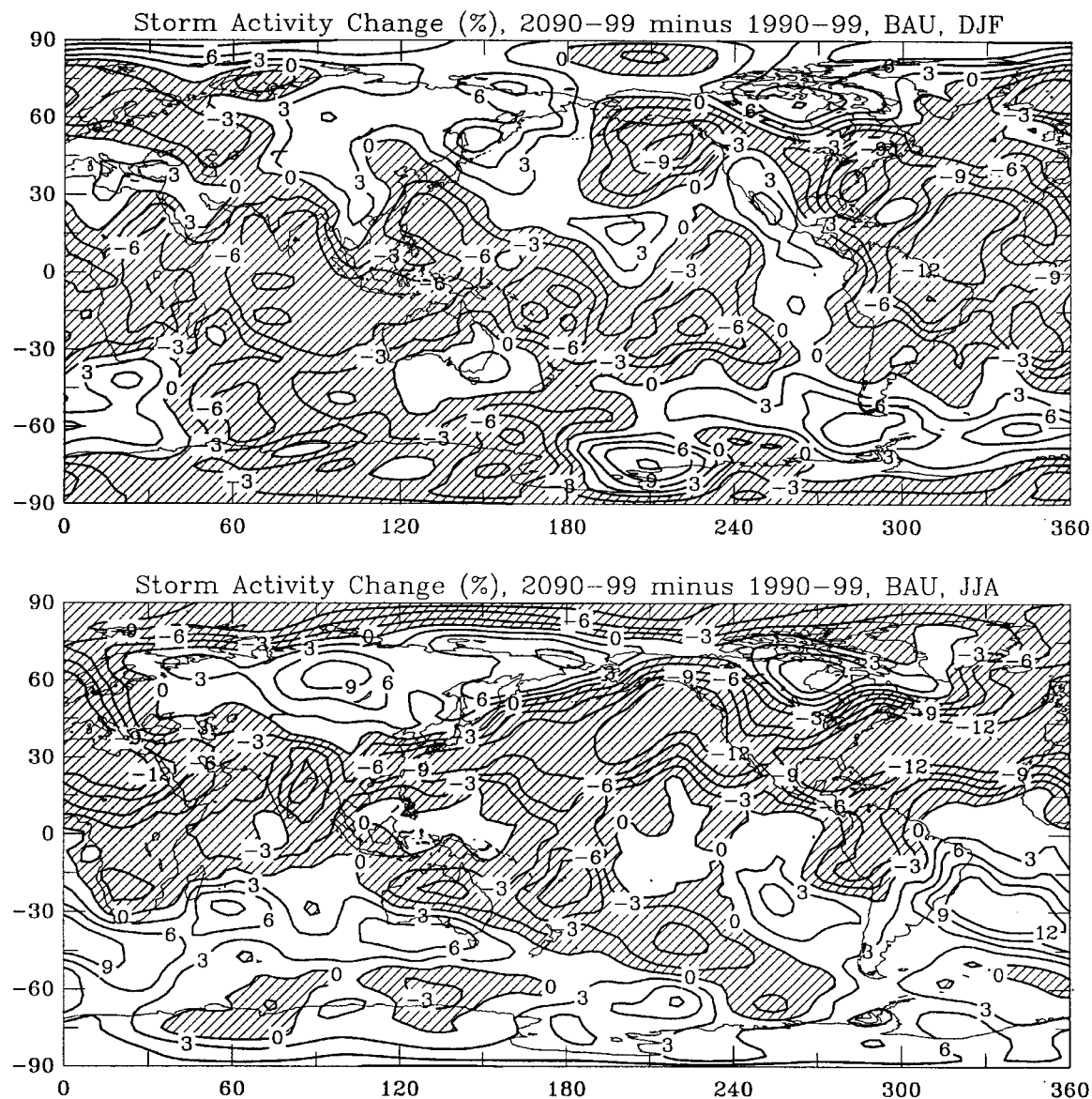


FIG. 33. Percentage change of CSM-simulated (top) DJF and (bottom) JJA standard deviation of bandpassed 2–8-day variations of surface pressure from 1990–99 to 2090–99 in the BAU run.

Ferrel cell over mid- to high latitudes also weakens by  $\sim 10\%$ – $15\%$ . Examination of the mean meridional cells for the 1990s and 2090s did not reveal any noticeable changes in the position of the cells.

A weakening of the Ferrel cell is expected from the decrease in the latitudinal temperature gradient (Fig. 21). The decrease in the overall intensity of the Hadley circulation, however, is not what one would anticipate from the increase in tropical surface temperatures (SST increases are similar to the surface air temperature changes shown in Fig. 19), nor from changes in latitudinal temperature gradient over low latitudes (which are small, see Fig. 21). The explanation appears to be as follows. GCM sensitivity experiments (Wang and

Rossow 1998) show that moving clouds from the mid-troposphere to either the upper or lower troposphere increases atmospheric static stability and reduces latent heating in the Tropics, resulting in a weakened Hadley circulation. In the CSM, these processes also operate: there is an upward shift in cloudiness (Fig. 31) and an increase in overall static stability in the Tropics (mostly over the oceans; Figure 22), which suppresses tropical convection<sup>4</sup> and thus the Hadley circulation.

<sup>4</sup> However, there are noticeable regional variations in stability changes (not shown) within the Tropics, and the convection around  $5^{\circ}$ – $8^{\circ}$  from the equator increases rather than decreases.



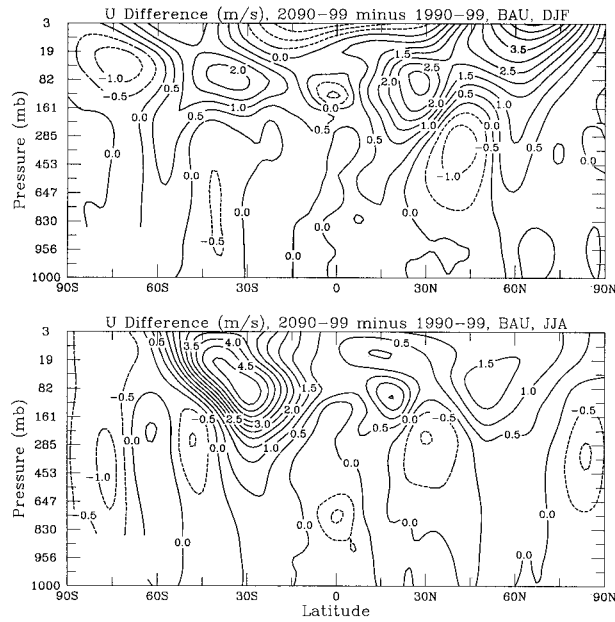


FIG. 34. Latitude–height distribution of zonal wind change ( $\text{m s}^{-1}$ ) from the 1990s to the 2090s in the BAU run averaged over longitude for (top) DJF and (bottom) JJA.

We do not know whether the weakening of the Hadley circulation that we see in our simulations is a common feature in future climate simulations, since circulation changes in response to increased atmospheric  $\text{CO}_2$  are seldom discussed in detail in other GCM studies and are not included in the 1990 and 1995 IPCC reports. The Hadley circulation does, however, also weaken in at least one other GCM (the GISS GCM, A. D. Del Genio 1999, personal communication). Recently, there have been reports of “El Niño-like” climate responses to increased atmospheric  $\text{CO}_2$  characterized by greater warming of SSTs in the eastern tropical Pacific compared to the western Pacific (Meehl and Washington 1996; Knutson and Manabe 1998; Boer et al. 2000; Timmermann et al. 1999; Meehl et al. 2000a). The CSM does not show such response in either the BAU or the STA550 simulation. This is consistent with CSM results from a simulation with 1% per year  $\text{CO}_2$  increase (Meehl et al. 2000a). Meehl et al. (2000a) attribute the lack of an El Niño-like response to negative net cloud forcing over the eastern tropical Pacific. Since cloud forcing is not well simulated in current GCMs (Cess et al. 1996), an El Niño-like response (or lack of such a response) is likely to be a model-dependent feature and therefore should be interpreted with caution. Since the Hadley circulation intensifies during El Niño events in the current climate (Oort and Yienger 1996), a true El Niño-like response should include strengthening of the Hadley circulation.

## 6. Summary and conclusions

The CSM produces a stable climate (except for the deep oceans) without the need for flux adjustments that

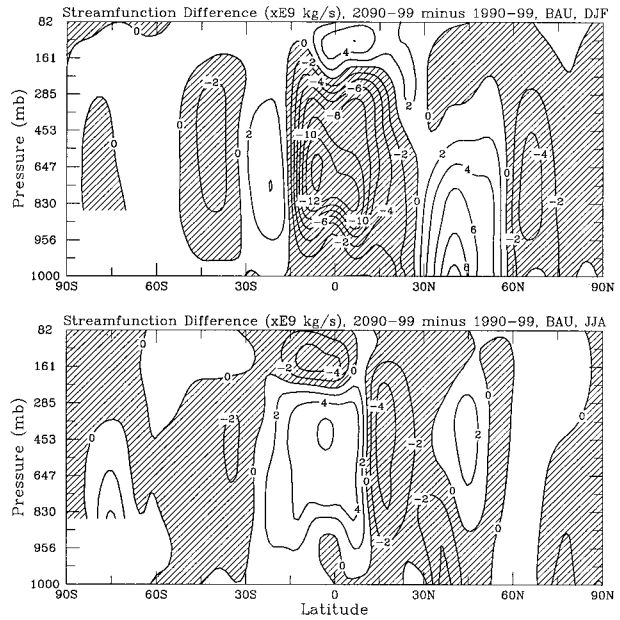


FIG. 35. Same as Fig. 34, but for the mean meridional streamfunction ( $10^9 \text{ kg s}^{-1}$ ). Negative values are hatched.

are used in many other coupled GCMs (Kattenberg et al. 1996). Using observed historical greenhouse gas concentrations and sulfate aerosol loadings, the CSM simulates many of the spatial and temporal variations of the twentieth-century climate. Specifically, the CSM simulates the following reasonably well: 1) geographical, seasonal, and year-to-year variations in global surface air temperature and precipitation; 2) latitude–height

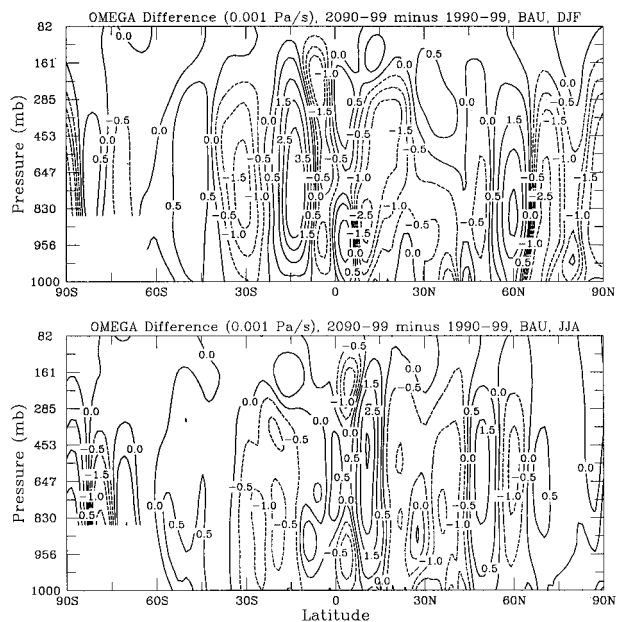


FIG. 36. Same as Fig. 34, but for vertical pressure velocity  $\omega$  ( $10^{-3} \text{ Pa s}^{-1}$ ). Negative contours are dashed.

distributions of zonal mean air temperature, specific humidity, and winds (including the regions of vertical motion that characterize the Hadley and Ferrel cells); 3) global distributions of 2–8-day synoptic storms; 4) ENSO-induced precipitation anomalies over the globe; 5) the Pole–midlatitude oscillations (such as the NAO) in sea level pressure fields; 6) the rapid rise in global and zonal mean surface temperatures since the late 1970s; and 7) increasing precipitation over northern mid- and high-latitude land areas during the twentieth century.

The CSM also has a number of systematic biases in simulating current climate. These include 1) a cold bias ( $2^{\circ}$ – $6^{\circ}\text{C}$ ) in surface air temperature over land areas, 2) overestimates of cloud amount (by 10%–30%) over land areas, 3) underestimates of cloud amount over the marine stratus regions west of North and South America and Africa, 4) reduced variability of equatorial Pacific SSTs and overestimates of tropical precipitation south of the equator in the Pacific, 5) a cold bias in the simulated surface air temperature at  $50^{\circ}$ – $70^{\circ}\text{N}$  from the 1920s to the 1940s (which may be partly due to absence of solar forcing in the simulations), and 6) a negative (positive) bias in surface (deep) ocean salinity, and excess sea ice in the North Pacific and the subarctic North Atlantic Oceans.

Some of these biases and other problems in the CSM are discussed in more detail in the papers published in the June 1998 issue of *Journal of Climate*. While the model still needs to be improved, the current version represents a major step forward in our efforts to simulate the climate system realistically. Therefore, we applied the CSM to simulate the climate of the twenty-first century under two different scenarios for future greenhouse gas concentrations and sulfur dioxide emissions, a business as usual case, and a  $\text{CO}_2$  stabilization case. In both cases, we used a future  $\text{SO}_2$  emissions scenario that is more realistic than any used previously in similar studies. We recognize that these simulations of future climate change have large uncertainties, which exist both in the forcing scenarios and in the model response to the forcing.

The two scenarios—business-as-usual (ACACIA-BAU) and  $\text{CO}_2$  stabilization (STA500)—were derived using the energy economics model (MiniCAM). They differ only in the atmospheric content of  $\text{CO}_2$ . Under the BAU scenario, the rise in atmospheric  $\text{CO}_2$  concentration accelerates slightly in the next century to reach about 710 ppmv by 2100 (approximately a doubling of the present value) mainly because of economic growth in developing countries and in world population. Under the STA550 scenario, it is assumed that certain policies will be implemented to gradually level off the  $\text{CO}_2$  concentration to stabilize at 550 ppmv by 2150. In both scenarios, industrial sulfate emissions peak in the first decade of the next century and then decrease gradually to less than half of present levels by 2100, pri-

marily as a result of increasing efforts to reduce acid deposition and air pollution.

The spatial patterns of climate change are generally similar under the two scenarios, with slightly smaller magnitudes under the STA550 scenario. Regional differences result largely from interdecadal variability. Beneath this variability, the signals of climate change over the twenty-first century are generally close to linear. We therefore summarize only the changes from the 1990s to the 2090s.

The CSM predicts substantial global mean warming of surface air temperature ( $\sim 1.9^{\circ}\text{C}$  in the BAU case and  $1.5^{\circ}\text{C}$  in the STA550 case) by 2099 (Fig. 17). Consistent with other coupled GCMs, the warming is largest over winter high latitudes ( $\geq 5.0^{\circ}\text{C}$ ) and smallest ( $\sim 1.0^{\circ}\text{C}$ ) over the southern oceans (around  $60^{\circ}\text{S}$ ; Table 1 and Fig. 19). By 2099 under the BAU scenario, annual surface air temperature increases by about  $1.5^{\circ}$ – $3.0^{\circ}\text{C}$  over most land areas and by about  $1.0^{\circ}$ – $2.0^{\circ}\text{C}$  over the oceans, except for the regions covered with sea ice during winter (e.g., the subarctic North Atlantic) where the warming is  $2^{\circ}$ – $5^{\circ}\text{C}$ . The warming in surface temperature is steady and surpasses the level of internal variability of the climate system by the early decades of next century (Figs. 17 and 18). Over low and midlatitudes, the warming is larger in the upper troposphere than in the lower troposphere (Fig. 19). This differential warming is not simply a result of increased latent heating, it results at least partly from the increased cloudiness and water vapor in the upper troposphere in a warmer climate (see below). Substantial cooling (up to  $5^{\circ}\text{C}$  in the BAU case) occurs in the midstratosphere as a result of enhanced radiative cooling by  $\text{CO}_2$ . In the lower stratosphere, however, particularly at mid–high southern latitudes, there is a warming associated with recovery of the ozone layer (as a result of the reduction in chlorofluorocarbons). Compared with the BAU scenario, the STA550 scenario reduces the tropospheric warming by  $\sim 0.5^{\circ}\text{C}$  and the stratospheric cooling by  $\sim 1.0^{\circ}$ – $2.0^{\circ}\text{C}$  by 2099 (Fig. 20).

The global mean precipitation rate increases under both the BAU ( $\sim 3.5\%$ ) and STA550 ( $\sim 3.0\%$ ) scenarios from the 1990s to the 2090s (Fig. 24), generally following the warming trends in global mean surface temperature. Coherent patterns of increasing precipitation (up to 50% increase) occur over northern mid- and high latitudes (especially in winter; Fig. 27), as a result of increased water vapor in the atmosphere. Large precipitation increases (30%–50%) also occur over India and the Arabian Peninsula. Precipitation changes over the subtropics are small. In the Tropics, in the summer hemisphere, precipitation increases in the zone around  $5^{\circ}$  from the equator and decreases in the zone around  $10^{\circ}$ – $15^{\circ}$  from the equator. These tropical precipitation changes are associated with changes in the zonal mean vertical motion, which shows a general decrease of  $\sim 10\%$  in the intensity of the Hadley circulation (Fig. 36).

Surface evaporation increases steadily together with surface temperature at all latitudes except for  $60^{\circ}$ – $90^{\circ}\text{S}$ ,

where the changes are small (Fig. 29). A large portion of the increased evaporation at low latitudes is transported to the mid- and high latitudes through the atmosphere and returned to the surface through increased precipitation there. Increased equatorward transport of water in the ocean is also implied, thereby completing an enhanced (by  $\sim 30\%$ – $40\%$ ) global hydrological cycle.

Changes in soil moisture content are generally small (within  $\pm 3\%$ ) over most land areas. There is a slightly increase ( $\leq 3\%$ ) of soil moisture content at northern mid- and high latitudes during winter and in the annual mean in response to increased precipitation there. At low latitudes, soil moisture changes can be as large as  $10\%$ – $20\%$  over areas with large precipitation changes (cf. Fig. 27).

Atmospheric water vapor content increases by  $\sim 30\%$ – $50\%$  in the upper troposphere. In the lower troposphere the increase is  $\sim 10\%$  for both summer and winter, except for northern high latitudes in winter where the increase is  $\sim 30\%$ – $60\%$ .

Total cloud cover changes little in both the BAU and STA550 simulations. However, there is an upward shift of cloudiness that results in increases ( $\sim 0.5\%$ – $1.0\%$  of sky cover) of cloudiness around tropopause and comparable decreases lower in the atmosphere (Fig. 31), a common feature in many other GCMs. These increases in cloudiness (and the large percentage increases in water vapor) in the upper troposphere result from the increased penetration of moist convection under a warmer climate. Through longwave radiation, these cloud and water vapor increases contribute to the enhanced warming in the upper troposphere.

Surface diurnal temperature range (DTR) decreases by about  $0.2^\circ$ – $0.5^\circ\text{C}$  over most land areas, except for Australia, South Africa (JJA), and northern Africa (DJF), where the DTR increases by  $0.2^\circ$ – $1.0^\circ\text{C}$  from the 1990s to the 2090s. The DTR decreases over the mid-latitude continents are associated with increases in precipitation, low-level cloudiness, and soil moisture content.

In general, 2–8-day synoptic storm activity decreases (by up to  $10\%$ ) at low latitudes and over midlatitude oceans. Over much of Eurasia and northern Canada, however, storm activity increases (by  $3\%$ – $10\%$ ). The storm activity changes are correlated with precipitation change patterns over northern mid- and high latitudes in winter.

The cores of the subtropical jets move slightly up- and equator-ward, especially over the winter hemisphere (Fig. 34). The westerlies in the lower stratosphere over the winter hemisphere also strengthen (by  $\sim 10\%$ – $15\%$ ). Associated with reduced latitudinal temperature gradients over mid- and high latitudes, the wintertime Ferrel cell weakens (by  $10\%$ – $15\%$ ). The zonal mean Hadley circulation also weakens slightly (by  $\sim 10\%$ ), although the ascending motion around  $5^\circ$  from the equator in the summer hemisphere increases slightly (leading to the

zone of increased precipitation noted above). The upward shift of cloudiness and the associated enhanced warming in the tropical upper troposphere (mostly over oceans, cf. Fig. 22) increase the static stability and reduce net latent heating in the Tropics, thereby contributing to the weakening of the Hadley circulation. It is suggested that “El Niño-like” may be a misleading term for characterizing the greater warming over the eastern tropical Pacific in response to increased  $\text{CO}_2$  in some coupled GCMs, since the models may not produce the circulation changes associated with a typical El Niño (such as an intensified Hadley cell).

We should emphasize that the CSM-simulated climate changes over the next century, especially those of regional precipitation and atmospheric circulation changes, have large uncertainties and may be model dependent. The uncertainties can result from incomplete representations of the physics of cloud formation and precipitation in the model, the model’s internal climate variability, the chaotic nature of the climate on small scales, and assumptions used in deriving the greenhouse gas and aerosol scenarios. Ensemble runs have recently been used to reduce one of these uncertainty areas, that associated with model internal variability. In the CSM, internal variability may be roughly estimated by the variability exhibited in the control run, or the variability superimposed on the secular trends in simulated changes (cf. Figs. 17, 18, 24, and 25). The simulated warming and the zonal mean precipitation increases over mid- and high latitudes are well above the levels of internal variability. These changes, therefore, are most reliable at least in a qualitative sense. Our results, when combined with those from similar simulations using other coupled GCMs (e.g., Kattenberg et al. 1996; Mitchell et al. 1998; Timmermann et al. 1999; Russell and Rind 1999; Roeckner et al. 1999; Boer et al. 2000), should help in improving predictions for the climate of the next 100 years.

**Acknowledgments.** We thank Drs. Anthony D. Del Genio and Jerry Meehl for constructive discussions, Ronald J. Stouffer and another anonymous reviewer for their helpful comments, and Dave Stepaniak for sharing his codes for computing the streamfunctions. This work was supported by NSF Special Funds (NCAR CGD 98-110, Amendment #63) and the ACACIA Consortium [CRIEPI, Japan; EPRI, California; KEMA Nederland B.V., the Netherlands; and the National Center for Atmospheric Research (NCAR), Colorado.]

## REFERENCES

- Alcamo, J., A. Bouwman, J. Edmonds, A. Grübler, T. Morita, and A. Sugandhy, 1995: An evaluation of the IPCC IS92 emission scenarios. *Climate Change 1994: Radiative Forcing of Climate Change and An Evaluation of the IPCC IS92 Emission Scenarios*, J. T. Houghton et al., Eds., Cambridge University Press, 247–304.
- Barth, M. C., P. J. Rasch, J. T. Kiehl, C. M. Benkowitz, and S. E.



- Schwartz, 2000: Sulfur chemistry in the National Center for Atmospheric Research Community Climate Model: Description, evaluation, features, and sensitivity to aqueous chemistry. *J. Geophys. Res.*, **105**, 1387–1415.
- Boer, G. J., G. Flato, and D. Ramsden, 2000: A transient climate change simulation with greenhouse gas and aerosol forcing: Projected climate for the 21st century. *Climate Dyn.*, **16**, 427–450.
- Bonan, G., 1998: The land surface climatology of the NCAR Land Surface Model (LSM 1.0) coupled to the NCAR Community Climate Model (CCM3). *J. Climate*, **11**, 1307–1326.
- Boville, B. A., and P. R. Gent, 1998: The NCAR Climate System Model, version one. *J. Climate*, **11**, 1115–1130.
- , and J. W. Hurrell, 1998: A comparison of the atmospheric circulations simulated by the CCM3 and CSM1. *J. Climate*, **11**, 1327–1341.
- , J. T. Kiehl, P. J. Rasch, and F. O. Bryan, 2001: Improvements to the NCAR CSM-1 for transient climate simulations. *J. Climate*, **14**, 164–179.
- Bryan, F. O., B. G. Kauffman, W. G. Large, and P. R. Gent, 1996: The NCAR CSM flux coupler. NCAR Tech. Note 424, 50 pp.
- Capotondi, A., and W. R. Holland, 1998: Thermohaline circulation variability in the NCAR Climate System Model (CSM). NCAR Tech. Note 445, 58 pp.
- Cess, R. D., and Coauthors, 1996: Cloud feedback in atmospheric general circulation models: An update. *J. Geophys. Res.*, **101**, 12 791–12 794.
- Cubasch, U., K. Hasselmann, H. Höck, E. Maier-Reimer, U. Mikolajewicz, B. D. Santer, and R. Sausen, 1992: Time-dependent greenhouse warming computations with a coupled ocean-atmosphere model. *Climate Dyn.*, **8**, 55–69.
- Dai, A., 1996: Global precipitation variability and its relationship with other climate changes. Ph.D. dissertation, Department of Geological Sciences, Columbia University, 303 pp. [Available from Columbia University Libraries, 535 West 114th Street, New York, NY 10027.]
- , and T. M. L. Wigley, 2000: Global patterns of ENSO-induced precipitation. *Geophys. Res. Lett.*, **27**, 1283–1286.
- , I. Y. Fung, and A. D. Del Genio, 1997a: Surface observed global land precipitation variations during 1900–88. *J. Climate*, **10**, 2943–2962.
- , A. D. Del Genio, and I. Fung, 1997b: Clouds, precipitation and temperature range. *Nature*, **386**, 665–666.
- , K. E. Trenberth, and T. R. Karl, 1999: Effects of clouds, soil moisture, precipitation and water vapor on diurnal temperature range. *J. Climate*, **12**, 2451–2473.
- Delworth, T. L., J. D. Mahlman, and T. R. Knutson, 1999: Changes in heat index associated with CO<sub>2</sub>-induced global warming. *Climatic Change*, **43**, 369–386.
- Dlugokencky, E. J., K. A. Masarie, P. M. Lang, and P. P. Tans, 1998: Continuing decline in the growth rate of the atmospheric methane burden. *Nature*, **393**, 447–450.
- Easterling, D. R., and Coauthors, 1997: Maximum and minimum temperature trends for the globe. *Science*, **277**, 364–367.
- Edmonds, J., M. Wise, H. Pitcher, R. Richels, T. M. L. Wigley, and C. MacCracken, 1997: An integrated assessment of climate change and the accelerated introduction of advanced energy technologies: An application of MiniCAM 1.0. *Mitigation Adapt. Strat. Global Change*, **1**, 311–339.
- Gaffin, D. J., and R. J. Ross, 1998: Increased summertime heat stress in the US. *Nature*, **396**, 529–530.
- Garcia, R. R., and S. Solomon, 1994: A new numerical model of the middle atmosphere. Part 2: Ozone and related species. *J. Geophys. Res.*, **99**, 12 937–12 951.
- Gent, P. R., F. O. Bryan, G. Danabasoglu, S. C. Doney, W. R. Holland, W. G. Large, and J. C. McWilliams, 1998: The NCAR Climate System Model global ocean component. *J. Climate*, **11**, 1287–1306.
- Hack, J. J., J. T. Kiehl, and J. W. Hurrell, 1998: The hydrologic and thermodynamic characteristics of the NCAR CCM3. *J. Climate*, **11**, 1179–1206.
- Hansen, J., A. Lacis, D. Rind, G. Russel, P. Stone, I. Fung, R. Ruedy, and J. Lerner, 1984: Climate sensitivity analysis of feedback mechanisms. *Climate Processes and Climate Sensitivity*, *Geophys. Monogr.*, No. 29, Amer. Geophys. Union, 130–163.
- Hurrell, J. W., 1995: Decadal trends in the North Atlantic Oscillation: Regional temperatures and precipitation. *Science*, **269**, 676–679.
- , J. J. Hack, B. A. Boville, D. L. Williamson, and J. T. Kiehl, 1998: The dynamical simulation of the NCAR Community Climate Model version 3 (CCM3). *J. Climate*, **11**, 1207–1236.
- Jones, P. D., M. New, D. E. Parker, S. Martin, and I. G. Rigor, 1999: Surface air temperature and its changes over the past 150 years. *Rev. Geophys.*, **37**, 173–199.
- Kalnay, E., and Coauthors, 1996: The NCEP/NCAR 40-Year Reanalysis Project. *Bull. Amer. Meteor. Soc.*, **77**, 437–471.
- Kattenberg, A., and Coauthors, 1996: Climate models—Projections of future climate. *Climate Change 1995: The IPCC Second Assessment*, J. T. Houghton et al., Eds., Cambridge University Press, 285–358.
- Kiehl, J. T., J. J. Hack, G. B. Bonan, B. A. Boville, B. P. Briegleb, D. L. Williamson, and P. J. Rasch, 1996: Description of the NCAR Community Climate model (CCM3). NCAR Tech. Note 420, 152 pp.
- , —, —, D. L. Williamson, and P. J. Rasch, 1998: The National Center for Atmospheric Research Community Climate Model: CCM3. *J. Climate*, **11**, 1131–1150.
- , T. L. Schneider, R. W. Portmann, and S. Solomon, 1999: Climate forcing due to tropospheric and stratospheric ozone. *J. Geophys. Res.*, **104**, 31 239–31 254.
- , —, P. J. Rasch, M. C. Barth, and J. Wong, 2000: Radiative forcing due to sulfate aerosols from simulations with the National Center for Atmospheric Research Community Climate Model, Version 3. *J. Geophys. Res.*, **105**, 1441–1457.
- Knutson, T. R., and S. Manabe, 1998: Model assessment of decadal variability and trends in the tropical Pacific Ocean. *J. Climate*, **11**, 2273–2296.
- Leggett, J. A., W. J. Pepper, and R. J. Swart, 1992: Emissions scenarios for IPCC: An update. *Climate Change 1992: The Supplementary Report to the IPCC Scientific Assessment*, J. T. Houghton, B. A. Callander, and S. K. Varney, Eds., Cambridge University Press, 69–95.
- Lockwood, M., and R. Stamper, 1999: Long-term drift of the coronal source magnetic flux and the total solar irradiance. *Geophys. Res. Lett.*, **26**, 2461–2464.
- Manabe, S., and R. J. Stouffer, 1994: Multiple-century response of a coupled ocean-atmosphere model to an increase of atmospheric carbon dioxide. *J. Climate*, **7**, 5–23.
- , —, M. D. Spelman, and K. Bryan, 1991: Transient response of a coupled ocean-atmosphere model to gradual changes of atmospheric CO<sub>2</sub>. Part I: Annual mean response. *J. Climate*, **4**, 785–818.
- Meehl, G. A., and W. M. Washington, 1996: El Niño-like climate change in a model with increased CO<sub>2</sub> concentrations. *Nature*, **382**, 56–60.
- , and J. M. Arblaster, 1998: The Asian–Australian monsoon and El Niño–Southern Oscillation in the NCAR Climate System Model. *J. Climate*, **11**, 1356–1385.
- , W. D. Collins, B. Boville, J. T. Kiehl, T. M. L. Wigley, and J. M. Arblaster, 2000a: Response of the NCAR Climate System Model to increased CO<sub>2</sub> and the role of physical processes. *J. Climate*, **13**, 1879–1898.
- , G. J. Boer, C. Covey, M. Latif, and R. J. Stouffer, 2000b: The Coupled Model Intercomparison Project (CMIP). *Bull. Amer. Meteor. Soc.*, **81**, 313–318.
- Mitchell, J. F. B., 1989: The “greenhouse” effect and climate change. *Rev. Geophys.*, **27**, 115–139.
- , S. Manabe, V. Meleshko, and T. Tokioka, 1990: Equilibrium climate change and its implications for the future. *Climate Change: The IPCC Scientific Assessment*, J. T. Houghton, G. J. Jenkins, and J. J. Ephraums, Eds., Cambridge University Press, 131–172.

- , T. C. Johns, J. M. Gregory, and S. F. B. Tett, 1995: Climate response to increasing levels of greenhouse gases and sulfate aerosols. *Nature*, **376**, 501–504.
- , —, and C. A. Senior, 1998: Transient response to increasing greenhouse gases using models with and without flux adjustment. Hadley Centre Tech. Note 2, 15 pp. [Available from Hadley Centre for Climate Prediction and Research, Meteorological Office, London Road, Bracknell, Berkshire RG12 2SY, United Kingdom.]
- Nicholls, N., G. V. Gruza, J. Jouzel, T. R. Karl, L. A. Ogallo, and D. E. Parker, 1996: Observed climate variability and change. *Climate Change 1995: The IPCC Second Assessment*, J. T. Houghton et al., Eds., Cambridge University Press, 133–192.
- Öm, G., U. Hansson, and H. Rodhe, 1996: Historical worldwide emissions of anthropogenic sulfur: 1860–1985. Dept. of Meteorology, Stockholm University, Rep. CM-91. [Available from Dept. of Meteorology, Stockholm University, S-106 91 Stockholm, Sweden.]
- Oort, A. H., and J. J. Yienger, 1996: Observed interannual variability in the Hadley circulation and its connection to ENSO. *J. Climate*, **9**, 2751–2767.
- Osborn, T. J., and T. M. L. Wigley, 1994: A simple model for estimating methane concentration and lifetime variations. *Climate Dyn.*, **9**, 181–193.
- Prather, M., R. Derwent, D. Ehhalt, P. Fraser, E. Sanhueza, and X. Zhou, 1996: Radiative forcing of climate change. *Climate Change 1995: The Science of Climate Change*, J. T. Houghton et al., Eds., Cambridge University Press, 86–103.
- Rasch, P. J., M. C. Barth, J. T. Kiehl, S. E. Schwartz, and C. M. Benkowitz, 2000: A description of the global sulfur cycle and its controlling processes in the National Center for Atmospheric Research Community Climate Model, Version 3. *J. Geophys. Res.*, **105**, 1367–1385.
- Roeckner, E., L. Bengtsson, J. Feichter, J. Lelieveld, and H. Rodhe, 1999: Transient climate change simulations with a coupled atmosphere–ocean GCM including the tropospheric sulfur cycle. *J. Climate*, **12**, 3004–3032.
- Rossow, W. B., and R. A. Schiffer, 1991: ISCCP cloud data products. *Bull. Amer. Meteor. Soc.*, **72**, 2–20.
- Russell, G. L., and D. Rind, 1999: Response to CO<sub>2</sub> transient increase in the GISS coupled model: Regional coolings in a warming climate. *J. Climate*, **12**, 531–539.
- Santer, B. D., T. M. L. Wigley, T. P. Barnett, and E. Anyamba, 1996: Detection of climate change and attribution of causes. *Climate Change 1995: The IPCC Second Assessment*, J. T. Houghton et al., Eds., Cambridge University Press, 407–444.
- Schimmel, D., and Coauthors, 1996: Radiative forcing of climate change. *Climate Change 1995: The IPCC Second Assessment*, J. T. Houghton et al., Eds., Cambridge University Press, 65–132.
- Shea, D. J., 1986: *Climatological Atlas: 1950–1979*. NCAR Tech. Note 269, 35 pp.
- Smith, S. J., H. Pitcher, and T. M. L. Wigley, 2000: Global and regional anthropogenic sulfur dioxide emissions. *J. Geophys. Res.*, in press.
- Solanki, S. K., and M. Fligge, 1999: A reconstruction of total solar irradiance since 1700. *Geophys. Res. Lett.*, **26**, 2465–2468.
- Thompson, D. W., and J. M. Wallace, 1998: The Arctic Oscillation signature in the wintertime geopotential height and temperature fields. *Geophys. Res. Lett.*, **25**, 1297–1300.
- Timmermann, A., J. Oberhuber, A. Bacher, M. Esch, M. Latif, and E. Roeckner, 1999: Increased El Niño frequency in a climate model forced by future greenhouse warming. *Nature*, **398**, 694–697.
- Trenberth, K. E., and D. A. Paolino, 1980: The Northern Hemisphere sea level pressure data set: Trends, errors and discontinuities. *Mon. Wea. Rev.*, **108**, 855–872.
- , and T. J. Hoar, 1996: The 1990–1995 El Niño–Southern Oscillation event: Longest on record. *Geophys. Res. Lett.*, **23**, 57–60.
- , D. P. Stepaniak, and J. M. Caron, 2000: The global monsoon as seen through the divergent atmospheric circulation. *J. Climate*, **13**, 3969–3993.
- Wang, J., and W. B. Rossow, 1998: Effects of cloud vertical structure on atmospheric circulation in the GISS GCM. *J. Climate*, **11**, 3010–3029.
- Watson, R. T., H. Rodhe, H. Oeschger, and U. Siegenthaler, 1990: Greenhouse gases and aerosols. *Climate Change: The IPCC Scientific Assessment*, J. T. Houghton, G. J. Jenkins, and J. J. Ephraums, Eds., Cambridge University Press, 1–40.
- Weatherly, J. W., B. P. Briegleb, W. G. Large, and J. A. Maslanik, 1998: Sea ice and polar climate in the NCAR CSM. *J. Climate*, **11**, 1472–1486.
- Wigley, T. M. L., 1993: Balancing the carbon budget—Implications for projections of future carbon dioxide concentration changes. *Tellus*, **45B**, 409–425.
- , 1999: *The Science of Climate Change: Global and U. S. Perspectives*. Pew Center on Global Climate Change, 48 pp.
- , R. Richels, and J. A. Edmonds, 1996: Economic and environmental choices in the stabilization of atmospheric CO<sub>2</sub> concentrations. *Nature*, **379**, 240–243.
- Wood, R. A., A. B. Keen, J. F. B. Mitchell, and J. M. Gregory, 1999: Changing spatial structure of the thermohaline circulation in response to atmospheric CO<sub>2</sub> forcing in a climate model. *Nature*, **399**, 572–575.
- Woodward, W. A., and H. L. Gray, 1993: Global warming and the problem of testing for trend in time series data. *J. Climate*, **6**, 953–962.
- Xie, P., and P. A. Arkin, 1997: Global precipitation: A 17-year monthly analysis based on gauge observations, satellite estimates, and numerical model outputs. *Bull. Amer. Meteor. Soc.*, **78**, 2539–2558.